Laser amplification with a twist: Traveling-wave propagation and gain functions from throughout the cochlea

Christopher A. Shera
Eaton-Peabody Laboratory of Auditory Physiology, Massachusetts Eye & Ear Infirmary, 243 Charles Street, Boston, Massachusetts 02114 and Department of Otology & Laryngology, Harvard Medical School, Boston, Massachusetts 02115

(Received 28 May 2007; revised 20 August 2007; accepted 21 August 2007)

Except at the handful of sites explored by the inverse method, the characteristics—indeed, the very existence—of traveling-wave amplification in the mammalian cochlea remain largely unknown. Uncertainties are especially pronounced in the apex, where mechanical and electrical measurements lack the independent controls necessary for assessing damage to the preparation. At a functional level, the form and amplification of cochlear traveling waves are described by quantities known as propagation and gain functions. A method for deriving propagation and gain functions from basilar-membrane mechanical transfer functions is presented and validated by response reconstruction. Empirical propagation and gain functions from locations throughout the cochlea are obtained in mechanically undamaged preparations by applying the method to published estimates of near-threshold basilar membrane responses derived from Wiener-kernel (chinchilla) and zwuis analysis (cat) of auditory-nerve responses to broadband stimuli. The properties of these functions, and their variation along the length of the cochlea, are described. In both species, and at all locations examined, the gain functions reveal a region of positive power gain basal to the wave peak. The results establish the existence of traveling-wave amplification throughout the cochlea, including the apex. The derived propagation and gain functions resemble those characteristic of an active optical medium but rotated by 90° in the complex plane. Rotation of the propagation and gain functions enables the mammalian cochlea to operate as a wideband, hydromechanical laser analyzer.
 [DOI: 10.1121/1.2783205]

PACS number(s): 43.64.Kc, 43.64.Bt, 43.60.Pt [BLM] Pages: 2738–2758

I. INTRODUCTION

Apart from the spontaneous emission of amplitude-stabilized sounds (Bialek and Wit, 1984; Shera, 2003a), the strongest evidence for traveling-wave amplification in the mammalian cochlea comes from measurements of basilar-membrane motion analyzed using the "inverse method" (e.g., Zweig, 1991; de Boer, 1983, 1995b; de Boer and Nuttall, 2001). Although compelling within their domain, the method's conclusions are restricted to a limited number of surgically accessible measurement locations, all in the basal turns of the cochlea. Other than at the handful of sites probed by inverse analysis, the form and characteristics—indeed, the very existence—of traveling-wave amplification remain largely unknown. Uncertainties are especially pronounced in the apex, where response measurements lack the independent controls necessary for gauging damage to the preparation (reviewed in Robles and Ruggero, 2001). Perhaps as a result, apical studies report the gamut from physiologically vulnerable nonlinearities reminiscent of the base to signs of active attenuation rather than amplification (e.g., Cooper and Rhode, 1995; Rhode and Cooper, 1996; Khanna and Hao 1999; Zinn *et al.* 2000). Even if the various findings were reliable and consistent, neither mechanical nonlinearity nor physiological lability provides evidence for actual power gain (or loss).[1] What's needed is a way of determining in uncompromised preparations the characteristics of traveling-wave amplification throughout the cochlea.

A. Propagation and gain functions

At a functional level, the form and amplification of cochlear traveling waves are described by quantities known as propagation and gain functions. By way of introduction, consider a simpler, textbook example of wave propagation: the transverse vibration of a stretched string (e.g., Georgi, 1993; Zwiebach, 2004). When the driving force is sinusoidal, the displacement, $d(x,t)$, of a uniform semi-infinite string (Fig. 1) has the wave-like form

$$d(x,t) = d_0 e^{\gamma x} \cos(\omega t - \kappa x + \phi_0), \tag{1}$$

where $\omega = 2\pi f$, and d_0 and ϕ_0 are the initial amplitude and phase. The spatial pattern of the wave on the string is determined by the propagation and gain coefficients, denoted by κ and γ, respectively; both have dimensions of inverse length. The propagation coefficient, κ, determines the spatial period (or wavelength, λ) of the wave via the equation $\lambda = 2\pi/\kappa$. The gain coefficient, γ, characterizes the effects of energy gains or losses and thereby determines whether, and how rapidly, the wave amplitude increases or decreases as it travels. For example, when the string loses vibrational energy due to viscous damping, γ is negative and the wave amplitude, controlled by the factor $e^{\gamma x}$, diminishes with increasing x. In general, both the propagation and gain coefficients depend on frequency. For example, $\kappa(f) = 2\pi f/c$, where $c = \sqrt{T/\rho}$ is the constant wave speed, here determined by the ratio of string tension, T, and mass density, ρ. For conve-

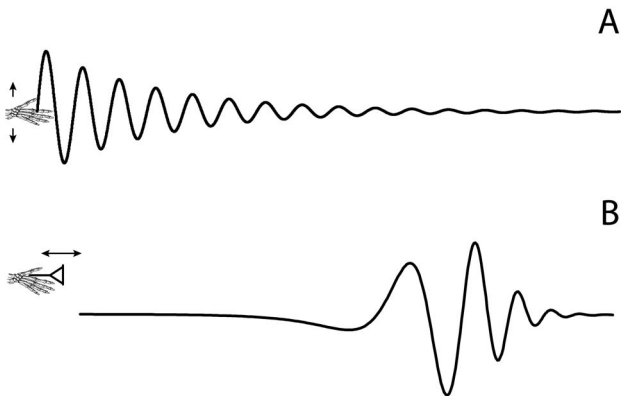

FIG. 1. Wave motion along a string and on the basilar membrane. The top panel (A) shows the transverse vibration of a uniform stretched string driven sinusoidally on the left. The propagation and gain coefficients determine the spatial pattern of the wave along the string. The change of wave amplitude reflects the sign of the string gain coefficient, γ. When the wave amplitude decreases with distance, as shown, the wave loses energy as it propagates (e.g., due to viscous damping in the surrounding medium), and $\gamma<0$. The bottom panel (B) shows the transverse vibration of the basilar membrane (BM) produced by sinusoidal motion of the stapes. Because the stiffness and other properties of the partition vary with position, the propagation and gain functions depend on x, and the sign of the gain function cannot simply be read off from the behavior of the wave envelope. For example, the declining stiffness of the partition causes BM vibration to increase to a maximum before decreasing, even when γ is everywhere negative (e.g., in a passive cochlea).

nience, κ and γ are often combined into a single complex number, k, known as the complex wavenumber and defined by $k \equiv \kappa + i\gamma$. The wave $d(x,t)$ can then be written in the more compact form

$$d(x,t) = \mathrm{Re}\{D_0 \exp i[\omega t - kx]\}, \tag{2}$$

where $D_0 \equiv d_0 e^{i\phi_0}$.

When the properties of the medium vary with position, as they do along a nonuniform string or within the cochlea, the waves manifest a somewhat more complicated relationship to the wave number. For example, the displacement of the basilar membrane (BM) produced by a pure tone has the approximate form

$$d_{\mathrm{BM}}(x,t) \cong \mathrm{Re}\left\{ D_0(f) \left[\frac{k(x,f)}{k(0,f)} \right]^{3/2} \times \exp i \left[\omega t - \int_0^x k(x',f)\,dx' \right] \right\}, \tag{3}$$

where the wave number $k(x,f)$ and its constituent propagation and gain functions $\kappa(x,f)$ and $\gamma(x,f)$ depend explicitly on position (e.g., Zweig *et al.*, 1976; de Boer, 1996). Although more intimidating in appearance than Eq. (2) for the wave on a uniform string, Eq. (3) for $d_{\mathrm{BM}}(x,t)$ is in many ways a straightforward generalization. The integral in the complex exponential simply sums the accumulating phase shift and gain as the wave propagates along. The prefactor out in front ($k^{3/2}$) arises because of energy conservation, which requires that the wave amplitude change when $k(x,f)$ changes, even in the absence of energy gains or losses (i.e., even when $\gamma=0$). In the cochlea, for example, the declining stiffness of the partition causes the wave speed and wavelength to decrease as the wave travels away from the stapes. As a result, the propagation function and prefactor increase with x, passively boosting the amplitude of vibration as the wave approaches its characteristic place. Although changes in wave amplitude are not so simply related to the sign of $\gamma(x,f)$ as they are on a uniform string, the gain function does determine the nature of power transfer to and from the wave. Regions of negative $\gamma(x,f)$ correspond to net power dissipation (e.g., via viscous losses within the organ of Corti); regions of positive $\gamma(x,f)$ correspond to power amplification.

B. Overview

Despite their significance for characterizing the form and power amplification of basilar-membrane traveling waves, the cochlear propagation and gain functions remain experimentally undetermined. Here we present a method for deriving propagation and gain functions from measurements of BM transfer functions. We apply the method to a variety of published estimates of BM motion, most notably to those obtained by (1) second-order Wiener-kernel analysis of chinchilla auditory-nerve-fiber (ANF) responses to near-threshold noise (Recio-Spinoso *et al.*, 2005) and (2) zwuis analysis of cat ANF responses to complex tones (van der Heijden and Joris, 2003, 2006). Both the Wiener-kernel (reviewed by Eggermont, 1993) and zwuis procedures estimate BM motion by extracting high-frequency timing information encoded in the neural response envelope by cochlear nonlinearities, principally the half-wave rectification that occurs at the inner hair cell synapse. When corrected for synaptic and neural transmission delays, the Wiener-kernel estimates closely resemble BM mechanical measurements made at corresponding locations and intensities (Temchin *et al.*, 2005). Because the broadband stimuli employed by the ANF-based procedures serve, in effect, to linearize the mechanical response (de Boer, 1997c; van der Heijden and Joris, 2006), the Wiener-kernel and zwuis measurements provide characterizations of cochlear tuning well suited to the linear inversion procedures employed here. Our analysis of the Wiener-kernel, zwuis, and other data determines cochlear propagation and gain functions throughout the cochlea.

II. THE INVERSION PROCEDURE

The inversion procedure described here uses measurements of the basilar-membrane traveling wave to find the cochlear propagation and gain functions.[2] At stimulus intensities in the linear regime near the threshold of hearing, the normalized mechanical response of the basilar membrane (e.g., BM velocity relative to stapes motion) depends on both the distance from the stapes, x, and the stimulus frequency, f. In the discussion that follows, we denote the normalized BM velocity by $V_{\mathrm{BM}}(x,f)$. Basilar-membrane traveling waves are iso-frequency slices of $V_{\mathrm{BM}}(x,f)$, and we denote the traveling wave at frequency f_{o} by $V_{\mathrm{BM}}(x,f_{\mathrm{o}})$, where the subscript "o" stands for "observation" and indicates that the stimulus frequency is regarded as a discrete parameter that is held constant (often at one of a relatively small number of values) while x varies continuously.

A. Finding traveling waves from transfer functions

With rare exceptions (e.g., von Békésy, 1960; Ren, 2002), BM mechanical responses are measured not as traveling waves but as transfer functions—not, that is, as $V_{BM}(x,f_o)$, a spatial response at fixed f_o, but as $V_{BM}(x_o,f)$, a frequency response at fixed x_o. To convert the transfer function $V_{BM}(x_o,f)$ at location x_o into an estimate of the traveling wave $V_{BM}(x,f_o)$ at frequency f_o, we apply the local scaling symmetry (Zweig, 1976) manifest by basilar-membrane transfer functions (Rhode, 1971; Gummer *et al.*, 1987) and neural tuning curves (e.g., Kiang and Moxon, 1974; Liberman, 1978). In its traditional form, local scaling implies that rather than depending on position and frequency independently, $V_{BM}(x,f)$ depends on the two variables x and f primarily in the dimensionless combination $\beta(x,f) \equiv f/\mathrm{CF}(x)$, where $\mathrm{CF}(x)$ is the characteristic frequency at location x (i.e., the cochlear position-frequency map). When the BM velocity scales, the function $V_{BM}[\beta(x,f)]$ describes both the transfer function and the traveling wave. In other words, frequency-domain measurements of the transfer function $V_{BM}(x_o,f)$, if plotted versus $f/\mathrm{CF}(x_o)$, provide spatial-domain measurements of the traveling wave $V_{BM}(x,f_o)$ plotted versus $f_o/\mathrm{CF}(x)$. If the scaling is local, the univariate description is most accurate in the region about the peak of the response [i.e., for x near x_o and for f near $\mathrm{CF}(x_o)$].

Figure 2 illustrates these remarks using an estimate of the BM click response at the 9-kHz place of the chinchilla cochlea obtained using second-order Wiener-kernel analysis of ANF responses to noise (Recio-Spinoso *et al.*, 2005). Panel (A) of Fig. 2 shows the Wiener-kernel estimate $v_{BM}(x_o,t)$ measured from a fiber with $\mathrm{CF}(x_o)=9$ kHz. In the time domain, scaling implies that BM click responses depend on x and t through the dimensionless combination $t \times \mathrm{CF}(x)$ representing time measured in periods of the local CF (Shera, 2001). Panel (B) shows the magnitude and phase of the transfer function $V_{BM}(x_o,f)$, found by computing the Fourier transform of the click response: $V_{BM}(x_o,f) = \mathcal{F}\{v_{BM}(x_o,t)\}$. The abscissa shows $\beta \equiv f/\mathrm{CF}(x_o)$ on a logarithmic axis. Local scaling implies that the same graph provides estimates of the envelope and phase lag of the traveling wave $V_{BM}(x,f_o)$ at frequency $f_o \cong \mathrm{CF}(x_o)$. To interpret the axis spatially, note that equal intervals along the axis represent equal intervals of space. (When the cochlear map is exponential, $\ln \beta$ is a linear function of x at fixed frequency.) Panel (C) shows a snapshot of the wave at one instant of time. Since they have units involving spikes/s that are not easily converted to those of velocity, Wiener-kernel estimates of BM velocity responses are customarily displayed in normalized form (Recio-Spinoso *et al.*, 2005).

1. Generalized local scaling in the apex

In many species, including the cat and chinchilla considered here, the cochlear position-frequency map deviates from a purely exponential form near its apical end (e.g., Liberman, 1982; Eldredge *et al.*, 1981; Greenwood, 1990). In these species, the map is better approximated by the "subtracted exponential"

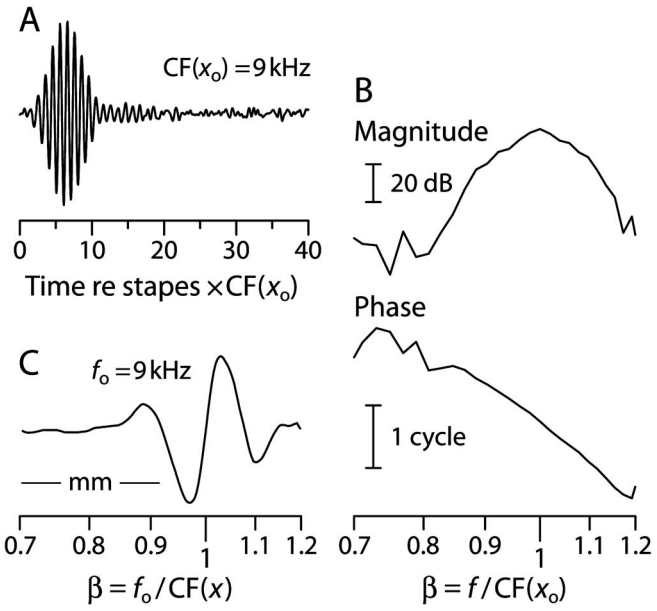

FIG. 2. (Panel A) Auditory-nerve based estimate of the BM click response, $v_{BM}(x_o,t)$, at the cochlear location x_o tuned to approximately 9 kHz in chinchilla (Recio-Spinoso *et al.*, 2005). The response estimate has been normalized by its peak value. Time, shown along the abscissa in units of the CF period, is measured relative to the approximate onset of stapes vibration by subtracting out estimates of acoustic and synaptic transmission delays amounting to a total of 1.225 ms (Temchin *et al.*, 2005). (Panel B) The magnitude and phase of the Fourier transform of $v_{BM}(x_o,t)$ provide an estimate of the BM mechanical transfer function, $V_{BM}(x_o,f)$, at the cochlear location x_o. Frequency, normalized by $\mathrm{CF}(x_o)=9$ kHz, increases along the logarithmic abscissa. (Panel C) Application of local scaling provides an estimate of the traveling wave by reinterpreting the abscissa $f/\mathrm{CF}(x)$ as a spatial axis at fixed frequency. The figure shows a snapshot of the 9-kHz wave whose envelope and phase are shown in Panel (B) The 1 mm scale bar is based on estimates of the chinchilla cochlear map (Eldredge *et al.*, 1981; Greenwood, 1990).

$$\mathrm{CF}(x) = [\mathrm{CF}(0) + \mathrm{CF}_1]e^{-x/l} - \mathrm{CF}_1, \tag{4}$$

which morphs from exponential to more linear behavior at characteristic frequencies near the transition frequency, CF_1.[3] We compensate for this apical deviation from the exponential map by working with a "generalized" local scaling variable that reduces to the traditional variable $\beta(x,f)$ in the base of the cochlea. This new scaling variable, denoted $\nu(x,f)$, is defined by

$$\nu(x,f) \equiv \frac{f + \mathrm{CF}_1}{\mathrm{CF}(x) + \mathrm{CF}_1} = \frac{\beta(x,f) + \beta_1(x)}{1 + \beta_1(x)}, \tag{5}$$

where $\beta_1(x) \equiv \mathrm{CF}_1/\mathrm{CF}(x)$. In the exponential portion of the cochlear map, the two variables $\beta(x,f)$ and $\nu(x,f)$ are nearly equivalent; the distinction becomes significant only at CFs lower than about two octaves above CF_1. (In the cat, $\mathrm{CF}_1 \cong 365$ Hz; in the chinchilla, $\mathrm{CF}_1 \cong 140$ Hz.)

The form of the generalized local scaling variable $\nu(x,f)$ was chosen to preserve the linear relation between x and $\ln \beta$ mentioned above: At fixed frequency, equal intervals of $\ln \nu$ correspond to constant distances along the BM. Use of the generalized scaling variable improves the validity of the local scaling approximation in the apex. When $V_{BM}(x,f)$ is approximated by a function of $\beta(x,f)$, the resulting transfer functions necessarily have the same quality factors (Q val-

FIG. 3. Spacetime slice through a symmetric, two-dimensional box model of height H. The x axis extends longitudinally from the base ($x=0$), and the y axis is oriented perpendicular to the basilar membrane, which spans the entire width, b, of the cochlea. The snapshot shown here has caught the BM participating in a traveling wave, whose vertical displacements have been hugely exaggerated for the purposes of illustration. The inversion procedure described in the text finds the wave's propagation and gain functions by analyzing measurements of the spatial displacement pattern.

ues) at all locations. But when $V_{\mathrm{BM}}(x,f)$ is approximated by a function of $\nu(x,f)$, the corresponding transfer functions are more broadly tuned (i.e., have smaller Q values) at more apical locations.[4] This broadening of tuning in the apex is qualitatively consistent with the trends observed experimentally (e.g., Liberman, 1978; Robles and Ruggero, 2001).

B. Finding propagation and gain functions from traveling waves

To find the wave number from the traveling wave we relate the two using a model of cochlear mechanics. We avoid unnecessary complication by working with the simplest geometry that manifests both long- and short-wave behavior. Figure 3 illustrates the linear, two-dimensional box model of the cochlea with incompressible and inviscid scala fluids. (With straightforward modifications the derivation reviewed below is easily extended to the three-dimensional model.) Basilar-membrane motion is driven by the antisymmetric (or difference) component of the pressure. By averaging the difference pressure over the scalae height and applying boundary conditions at the scalae walls and BM, one can show that the averaged difference pressure, $\bar{P}(x,f)$,[5] satisfies the one-dimensional wave equation

$$(\partial_x^2 + k^2)\bar{P} = 0, \tag{6}$$

where $k(x,f)$ is the complex wave number (Shera *et al.*, 2005; Duifhuis, 1988; Talmadge *et al.*, 2001).

To find $k(x,f)$ we note that the BM velocity $V_{\mathrm{BM}}(x,f)$ is related to the second spatial derivative of the pressure through the equation

$$\partial_x^2 \bar{P} = bZ_{\mathrm{f}}V_{\mathrm{BM}}, \tag{7}$$

where b is the BM width and $Z_{\mathrm{f}}(f)$ is the effective acoustic impedance of the fluids [notation adopted from Shera *et al.* (2005)]. If the function $V_{\mathrm{BM}}(x,f)$ is known—whether by model or by measurement—Eq. (7) can be solved for $\bar{P}(x,f)$ by double integration:

$$\bar{P}(x,f) = bZ_{\mathrm{f}}(f)\int_x^L dx' \int_{x'}^L V_{\mathrm{BM}}(x'',f)dx'', \tag{8}$$

where x' and x'' are dummy integration variables. The constants of integration are chosen to satisfy the boundary conditions (in this case, $\bar{P}=\partial_x\bar{P}=0$ at the helicotrema).[6] Combining Eqs. (6)–(8) and solving for the wave number yields

$$k^2(x,f) = -V_{\mathrm{BM}}(x,f) \Big/ \int_x^L dx' \int_{x'}^L V_{\mathrm{BM}}(x'',f)dx''. \tag{9}$$

This *wave number inversion formula* indicates how to find the complex wave number from the traveling wave. Derived in an earlier publication (Shera *et al.* 2005), Eq. (9) generalizes the long-wave procedure suggested by de Boer (1995a). The propagation and gain functions are then found by taking the real and imaginary parts of the wave number:

$$\kappa(x,f) = \mathrm{Re}\, k(x,f) \text{ and } \gamma(x,f) = \mathrm{Im}\, k(x,f). \tag{10}$$

The sign of the square root needed to obtain k from k^2 is set by the presumption that the wave travels forward in the vicinity of its peak [i.e., $\kappa(\nu\cong 1)>0$].[7]

Inversion formula (9) has a number of happy features that render it well suited to our application. First and foremost, the derived wave number $k(x,f)$ depends only on the given BM response function, $V_{\mathrm{BM}}(x,f)$, and is independent of the value of H, the effective height of the model. [Derived here using a 2D model, the inversion formula generalizes to 3D if $V_{\mathrm{BM}}(x,f)$ is understood as the velocity of the BM averaged over its width.] In other words, the function $V_{\mathrm{BM}}(x,f)$ yields the same wave number irrespective of whether the assumed hydrodynamic model is everywhere long wave or short wave, or manifests a transition between the two, as in the real cochlea. In addition, the inversion procedure does not assume that the measured $V_{\mathrm{BM}}(x,f)$ contains only a forward-traveling wave; contributions from both forward- and reverse-traveling components are allowed.[8] Furthermore, the procedure involves neither algorithmic iteration nor numerical differentiation of the measured response, both of which require special care and handling (Zweig, 1991) to suppress confounding magnification of error. Finally, note that Eq. (9) for $k^2(x,f)$ is independent of the overall magnitude of $V_{\mathrm{BM}}(x,f)$; any constant scale factor cancels in the ratio. The fact that the wave number depends on the shape and fine structure of the traveling wave, but not on its absolute scale, makes possible its determination from the indirect estimates of BM motion provided by Wiener-kernel and zwuis analysis.

Figure 4 shows the propagation and gain function $\kappa(\nu)$ and $\gamma(\nu)$ obtained from Eq. (9) using the Wiener-kernel estimate of the traveling wave $V_{\mathrm{BM}}(\nu)$ shown in Fig. 2. The spatial integrals were evaluated using the differential relation $d\nu/\nu = dx/l$, where $l\cong 3.8$ mm is the space constant of the chinchilla cochlear map (Eldredge *et al.*, 1981; Greenwood, 1990). Note that the derived propagation and gain functions become unreliable outside the peak region (i.e., at locations $|\nu-1|\gtrsim 0.2$ in this example), where noise contaminates the Wiener-kernel transfer function.

C. Validation by reconstruction

To validate the inversion procedure we used the Wentzel–Kramers–Brillouin (WKB) approximation to reconstruct the traveling wave from the derived wave number (e.g., Mathews and Walker, 1964; Zweig *et al.*, 1976). Combining the WKB solution to Eq. (6) for $\bar{P}(x,f)$ with Eq. (7) for $V_{\mathrm{BM}}(x,f)$ yields the formula

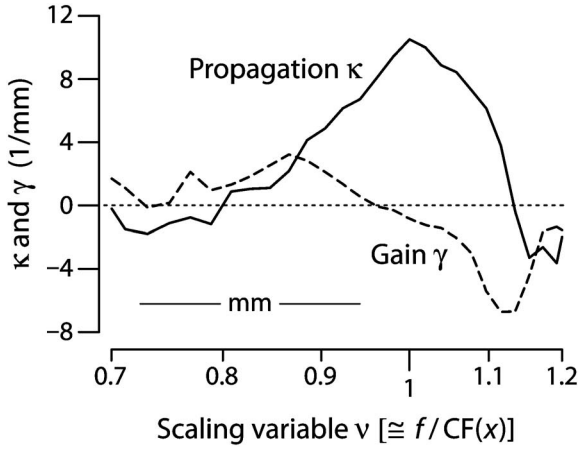

FIG. 4. Derived propagation and gain functions. Plotted vs the generalized scaling variable using solid and dashed lines, respectively, the functions $\kappa(\nu)$ and $\gamma(\nu)$ were obtained by inversion from the estimate of $V_{\mathrm{BM}}(\nu)$ shown in Fig. 2 (CF=9 kHz). Because $\mathrm{CF}_1 \ll 9$ kHz, ν is nearly equivalent to the normalized frequency $f/\mathrm{CF}(x)$. Parameters for the chinchilla cochlear map were taken from Greenwood (1990). For reference, thin dashes mark the zero line. The scale bar represents a distance of 1 mm.

$$V_{\mathrm{BM}}(x,f) \propto k^{3/2}(x,f)\exp\left[-i\int_0^x k(x',f)dx'\right], \tag{11}$$

where the proportionality factor depends on f. Readers may recognize the WKB formula from its earlier appearance in Eq. (3). Figure 5 shows that both the amplitude and the phase of the reconstructed response are in good agreement with the original. Thus, independent of their origin, the propagation and gain functions shown in Fig. 4 evidently provide a valid representation of the complex wave number of the traveling wave.

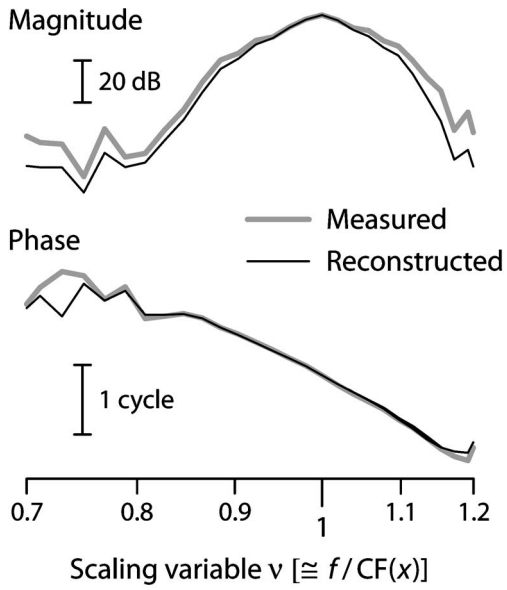

FIG. 5. Traveling wave/transfer function reconstructed from the derived wave number using the WKB approximation. The reconstructed response (thin solid line) was obtained from the wave number in Fig. 4 using the WKB formula [Eq. (11) for $V_{\mathrm{BM}}(x,f)$] and evaluating the integral using generalized scaling. An overall complex scale factor was determined by matching the data at the peak. For comparison, the original Wiener-kernel measurements are reproduced from Fig. 2 (thick gray line).

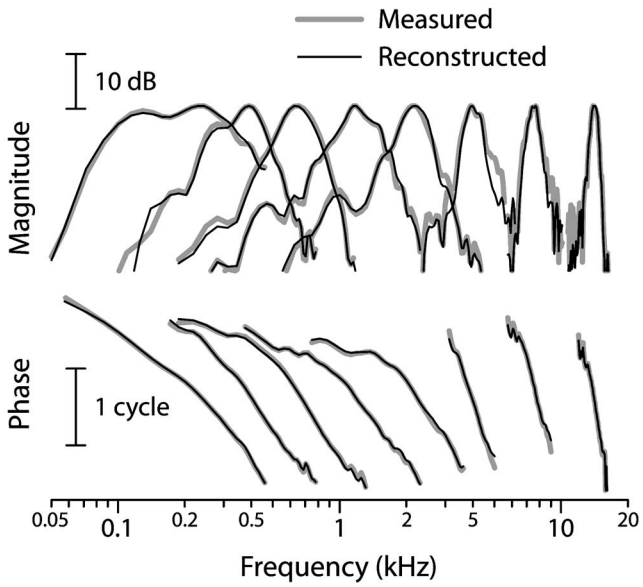

FIG. 6. Original and reconstructed Wiener-kernel transfer functions from locations throughout the chinchilla cochlea. Transfer functions are shown normalized to the same peak amplitude.

We applied the inversion and reconstruction procedure outlined above to each of the 137 near-threshold Wiener-kernel BM click responses used to assemble the recently published map of near-CF BM group delays (see Fig. 13 of Temchin *et al.* 2005). More than 60% of the Wiener kernels (86/137) yielded reconstructions judged satisfactory by visual inspection.[9] Unsuccessful reconstructions often contained anomalous spikes or other discontinuous behavior within the peak region. Similar problems can occur when inverting model responses if the boundary conditions assumed by the inversion formula are not well satisfied. Figure 6 shows typical comparisons of measured and successfully reconstructed transfer functions at CFs spanning the length of the chinchilla cochlea. The quality of the reconstructions demonstrates that the wave number inversion procedure can be successfully applied throughout the cochlea. For logical consistency, we restrict further attention to results obtained from wave numbers validated using the reconstruction procedure.

III. TRAVELING-WAVE PROPAGATION AND GAIN FUNCTIONS

A. Qualitative features

Figure 7 shows $\kappa(\nu)$ and $\gamma(\nu)$ successfully derived from nine Wiener-kernel estimates of $V_{\mathrm{BM}}(\nu)$ with CFs in the range 8–10 kHz (gray lines) together with trend lines that capture the mean behavior.[10] Although individual Wiener kernels and corresponding propagation and gain functions manifest considerable individual variability in their fine detail, all share the same qualitative form. Regarded as a function of position, the propagation functions $\kappa(\nu)$ start out small in the region basal to the wave peak ($\nu \lesssim 0.85$), increase to a maximum near the characteristic place ($\nu \cong 1$), and then decrease again beyond. (Equivalently, the wavelength starts out large near the stapes, decreases to a mini-

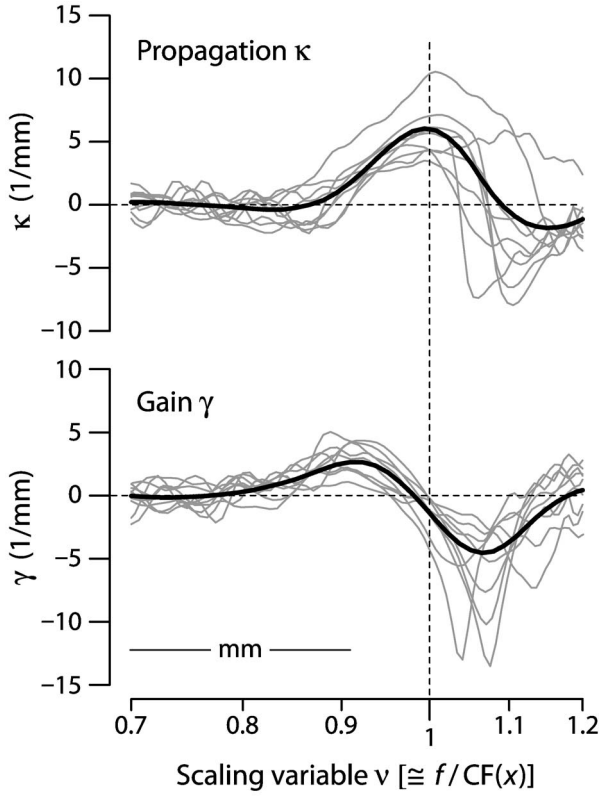

FIG. 7. Propagation and gain functions derived from all nine Wiener kernels with CFs in the range 8–10 kHz. Gray lines show individual functions $\kappa(\nu)$ and $\gamma(\nu)$; black lines show trends obtained by loess fitting (Cleveland, 1993). For reference, thin dashes mark the zero lines and the location of the wave peak ($\nu=1$). The scale bar represents a distance of 1 mm.

mum in the vicinity of the peak, and then increases in the apical "cutoff" region where the wave amplitude decreases rapidly.) At even more apical locations, κ generally passes through zero and goes slightly negative, beyond which the Wiener kernels are generally too noisy to provide reliable trends. The decrease in κ apical to the best place reflects the severe attenuation of the response in this region as the wave transitions from traveling to evanescent behavior (see Sec. IV B 3).

Like the propagation functions, the gain functions also manifest pronounced spatial dispersion (i.e., they vary considerably with x at fixed frequency). In particular, $\gamma(\nu)$ starts out close to zero, where its sign is poorly determined, and increases to a maximum located basal to the wave peak ($\nu \cong 0.9$). The gain function then decreases, passes through zero near $\nu=1$, and becomes negative in the cutoff region.

Because of the assumed local scaling, the spatial perspective adopted above can be flipped and the horizontal axis in Fig. 4 regarded instead as a frequency axis at fixed position. Viewed in this complementary way, strong spatial dispersion becomes strong frequency dispersion. The figure then shows that the propagation and gain functions at the 9 kHz place start out small and increase with the frequency of stimulation. Whereas the propagation function increases all the way to CF and then decreases at higher frequencies, the gain function peaks at a frequency below CF and then reverses sign as it passes through zero near CF.

1. Interpretation in terms of energy flow

To interpret the form of the gain function we note that energy conservation implies that at every location the power transferred by the organ of Corti to the fluid must be the negative of that expended moving the partition. Consequently, when the scalae fluids are assumed inviscid the time-averaged power per unit BM area transfered to the traveling pressure-difference wave is given by

$$w(x,f) = -\tfrac{1}{2}\,\mathrm{Re}\,P_0 V_{\mathrm{BM}}^{*}, \tag{12}$$

where the quantity $P_0(x) \equiv P(x, y=0^+)$ is the pressure difference driving the cochlear partition.[11] Equation (12) can be rewritten in terms of the BM velocity and impedance by using the relation $P_0 = bZ_{\mathrm{BM}}V_{\mathrm{BM}}$:

$$w(x,f) = -\tfrac{1}{2}b|V_{\mathrm{BM}}|^2\,\mathrm{Re}\,Z_{\mathrm{BM}}. \tag{13}$$

In the shortwave regime near the response peak, the BM impedance and wave number are related by $Z_{\mathrm{BM}} = -Z_{\mathrm{f}}H/k$.[12] Hence,

$$w(x,f) = -\omega\rho_0|V_{\mathrm{BM}}|^2\,\mathrm{Im}\,\frac{1}{k} = \omega\rho_0\left|\frac{V_{\mathrm{BM}}}{k}\right|^2\gamma, \tag{14}$$

where we have used the definition $Z_{\mathrm{f}} = 2i\omega\rho_0/bH$ (Shera *et al.*, 2005). Note that $\mathrm{sign}(w) = \mathrm{sign}(\gamma)$. In other words, the direction of power transfer to or from the traveling wave is determined by the sign of the gain function, γ. Negative gain functions ($\gamma<0$) correspond to net wave power absorption by the organ of Corti; positive gain functions ($\gamma>0$) correspond to net wave power amplification.

Equation (14) and local scaling enable us to interpret the empirical gain functions shown in Fig. 7 in terms of power flow. Near the 9 kHz place, the derived gain functions imply that the organ of Corti amplifies waves of corresponding frequency as they travel towards their characteristic place and squelches them beyond. Viewed from the complementary perspective of frequency, the CF place amplifies waves with frequencies less than CF and attenuates those with frequencies greater than CF.

The existence of power amplification at high CFs corroborates features of the BM impedance obtained by applying the inverse method to mechanical transfer functions from the base of the cochlea (e.g., Zweig, 1991; de Boer, 1995b; de Boer and Nuttall, 2001). In both species previously examined (squirrel monkey and guinea pig), the BM impedance was found to manifest a bowl-shaped region of negative resistance just basal to the response peak. Since regions of negative resistance correspond to regions of positive γ (see Sec. IV B 3), our findings from the basal end of the chinchilla cochlea are consistent with these previous results.

B. Generalization to other locations, species, and measurements

Employing ANF-derived estimates of cochlear tuning allows us to extend the analysis of cochlear propagation and gain throughout the cochlea. Figures 8–10 demonstrate that the qualitative features of the derived propagation and gain functions evident in Fig. 7 apply not just to chinchilla responses near the 9 kHz place but to cochlear traveling waves

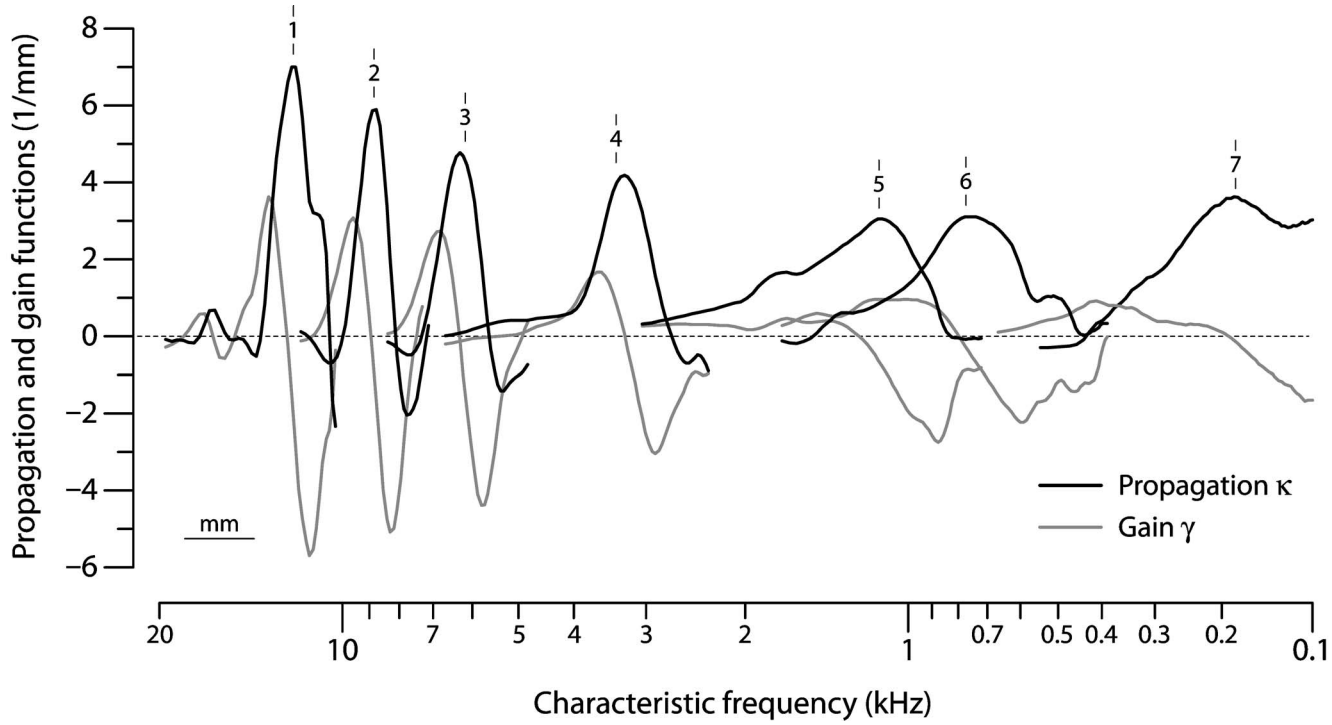

FIG. 8. Propagation and gain trends throughout the cochlea. The figure shows trend functions $\kappa(x,f_n)$ and $\gamma(x,f_n)$ at seven frequencies f_n spanning the frequency range of the chinchilla cochlea. Trend functions were computed as described for Fig. 7 by binning the 86 reconstructed Wiener kernels into seven CF groups with bin edges of $\{16,10,8,5,2,1,0.5,0.1\}$ kHz. The results are plotted on a spatial axis converted to equivalent CF using an estimate of the chinchilla cochlear map (Eldredge *et al.*, 1981; Greenwood, 1990). The nth pair of functions is plotted at the location where $\mathrm{CF}(x_n)=f_n$, where f_n is the geometric mean CF of the group. Short vertical lines, indexed by integers ($n=1,2\ldots,7$) for future reference, identify the nominal frequency f_n of each group. The trend values at the 9-kHz site ($n=2$) appeared earlier in Fig. 7. The scale bar represents a distance of 1 mm. For reference, thin dashes mark the zero line.

more generally. Figure 8 illustrates traveling-wave propagation and gain functions derived from Wiener-kernel responses throughout the chinchilla cochlea. The figure shows trend values of $\kappa(x,f_n)$ and $\gamma(x,f_n)$ on a spatial axis expressed in equivalent CF using the cochlear map; functions are shown at seven nominal frequencies $f_{n=1,2,\ldots,7}$ spanning the frequency range of chinchilla hearing. The functions were computed by binning the propagation and gain functions from the 86 successfully reconstructed Wiener kernels into seven CF groups, sliding each to align the CFs using the generalized scaling variable $\nu(x,f_n)$, and performing loess fits to each aligned ensemble. For example, the trend values shown above in Fig. 7 are reproduced at $\mathrm{CF}(x_2)=9$ kHz.

To facilitate comparisons across CF, Fig. 9 collapses the trend functions shown spread along the cochlea in Fig. 8 onto a common center by replotting them as a function of the generalized local scaling variable, ν. Although quantitative details vary (see below), propagation and gain functions evidently share the same qualitative form throughout the cochlea. For example, gain functions at locations from base to apex all manifest extended regions of power amplification and absorption located on opposite sides of the response peak.

We found similar results in other species by inverting tuning measurements obtained using different techniques. For example, propagation and gain functions derived from published estimates of $V_{\mathrm{BM}}(x_o,f)$ in cat obtained from auditory-nerve responses to zwuis stimuli (van der Heijden and Joris, 2003, 2006) have the same qualitative form as those derived from the chinchilla Wiener kernels. Figure 10 illustrates these remarks by showing the functions $\kappa(\nu)$ and $\gamma(\nu)$ obtained from the apex of the cat cochlea (CF <1 kHz); similar functions are obtained from more basal locations (not shown). Evidently, propagation and gain functions in the cat cochlea share the same basic form as those in the chinchilla (cf. Figs. 7 and 8). Likewise in the gerbil, a species for which we obtained similar results by applying the wave number inversion procedure both to direct mechanical measurements of the traveling wave (Ren, 2002) and to frequency-domain transfer functions (de La Rochefoucauld and Olson, 2007). In the latter case, the recovered gain functions lacked the prominent region of positive gain basal to the wave peak, consistent with the presumed passive status of the preparation.

C. Variation along the cochlea

Although the derived propagation and gain functions have the same qualitative form throughout the cochlea, quantitative details vary systematically with characteristic frequency.

1. Near-peak and maximum values

The trend functions shown in Figs. 8 and 9 suggest that peak values of the propagation function are largest in the base of the cochlea and decrease at locations further from the stapes. Figure 11 corroborates this trend with a scatterplot showing values of $\hat{\kappa}\equiv\kappa(\nu=1)$ for all 86 successfully derived

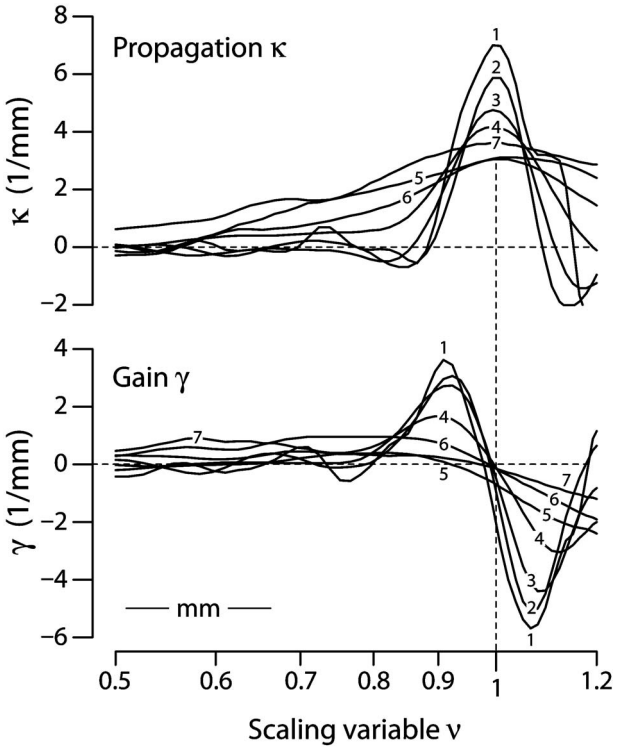

FIG. 9. Superposed propagation and gain functions from throughout the cochlea. The figure shows the trend functions $\kappa(x,f_o)$ and $\gamma(x,f_o)$ from Fig. 8 superposed by plotting them versus the generalized scaling variable, $\nu \equiv [f+\mathrm{CF}_1]/[\mathrm{CF}(x_n)+\mathrm{CF}_1]$. The integer labels ($n=1,2,\ldots,7$) correspond to those used in Fig. 8. The horizontal ν axis differs significantly from $\beta = f/\mathrm{CF}(x_n)$ only for curve $n=7$ from the extreme apex. The scale bar represents a distance of 1 mm. For reference, thin dashes mark the zero lines and the location of the wave peak ($\nu=1$).

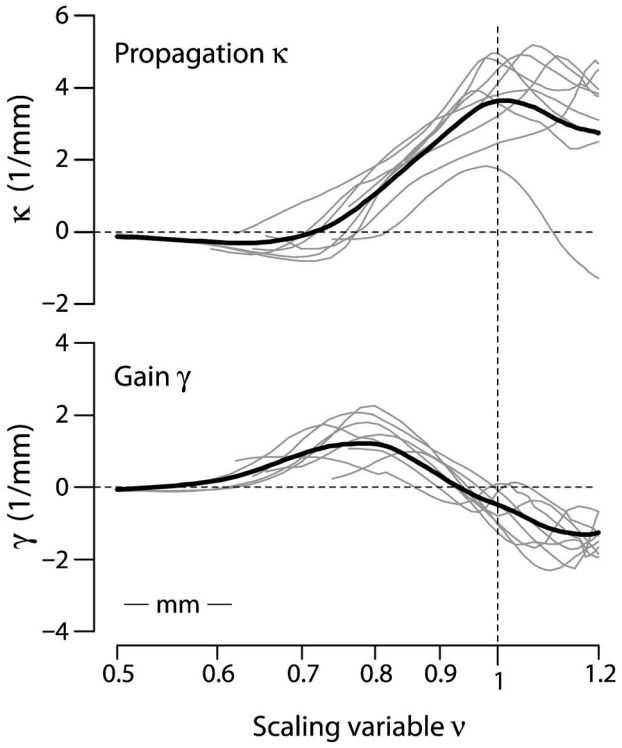

FIG. 10. Propagation and gain functions derived from estimates of $V_{\mathrm{BM}}(x_o,f)$ from the apex of the cat cochlea (CFs less than 1 kHz) obtained by van der Heijden and Joris (2006). Gray lines show individual functions $\kappa(\nu)$ and $\gamma(\nu)$; black lines show corresponding trends obtained by loess fitting. The scale bar represents a distance of 1 mm. For reference, thin dashes mark the zero lines and the location of the wave peak ($\nu=1$).

propagation functions in chinchilla. The decrease in $\hat{\kappa}$ implies that the wavelength at the peak ($\hat{\lambda} \equiv 2\pi/\hat{\kappa}$) increases by a factor of 3–4 from base to apex, from a minimum near the stapes of about 0.5–0.6 mm (i.e., 50–60 rows of hair cells) to a maximum of about 1.6–2 mm (160–200 rows) in the apex. These values of the near-peak wavelength correspond well with estimates obtained from mechanical phase data measured at nearby sites along the BM, at least at the handful of locations where such measurements have proved possible (Robles and Ruggero, 2001, Table IV). In addition to corroborating the overall trend apparent in Figs. 8 and 9, the scatterplot in Fig. 11 provides an indication of the substantial variability in $\hat{\kappa}$ associated with individual Wiener kernels.

Since the data are relatively sparse below 1 kHz, apical trends should be viewed with caution. (Because the cochlear map is more linear in the apex, the apical end also occupies a somewhat disproportionate space on the logarithmic axes of the graph.) Contributing to the uncertainty are doubts about the validity of generalized local scaling and the reliability of the cochlear map, both of which are not as well characterized in the apex. The dotted lines in Fig. 11 provide a measure of these uncertainties by showing how overall trends in $\hat{\kappa}$ change when the propagation and gain functions are derived by using traditional rather than generalized scaling (i.e., by using β rather than ν as the independent variable). The use of traditional scaling converts a shallow apical upturn in $\hat{\kappa}$ into a monotonic decline throughout the cochlea. Notwithstanding these uncertainties, the apical upturn predicted by generalized scaling appears consistent with the behavior of the near-peak wavelength obtained from spatial phase patterns reconstructed from neural measurements in cat (van der Heijden and Joris, 2006).

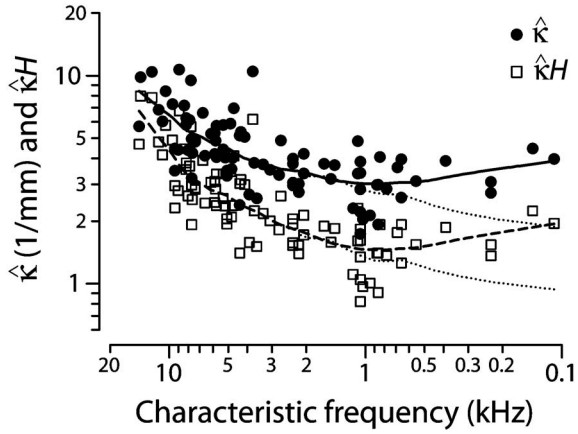

FIG. 11. Scatterplots of $\hat{\kappa}$ and $\hat{\kappa}H$ from throughout the chinchilla cochlea. The black dots give values of $\hat{\kappa}$, defined as the value of the propagation function at the wave peak ($\nu=1$), vs characteristic frequency. Values are shown for all 86 successfully reconstructed Wiener kernels. The open squares give values of $\hat{\kappa}H$, where H is the effective height of the scalae, defined as the radius of the equivalent circle (area equal to the combined areas of the scala vestibuli and tympani) as computed from measured scalae dimensions (Salt, 2001). Values $\hat{\kappa}H > 1$ imply that the hydrodynamics at the peak is short wave. The solid and dashed lines are loess trend lines (Cleveland, 1993) superposed to guide the eye. The dotted lines show trends computed from propagation functions derived using traditional rather than generalized local scaling.

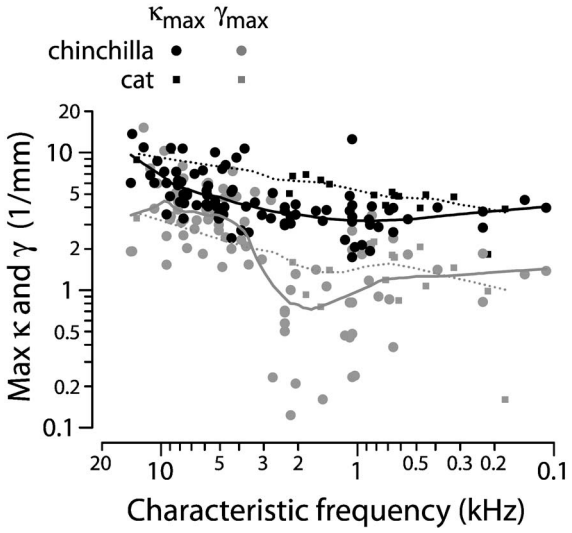

FIG. 12. Scatterplot of the maximum values of κ and γ versus CF. Black symbols show values of $\kappa_{\max}$ in chinchilla (circles) and cat (squares); gray symbols show corresponding values of $\gamma_{\max}$. Loess trends for chinchilla and cat are shown with solid and dotted lines, respectively.

Figure 12 shows the variation of the maximum values of the propagation and gain functions. The points represent values of $\kappa_{\max} \equiv \max(\kappa)$ and $\gamma_{\max} \equiv \max(\gamma)$ versus CF for both chinchilla and cat. Since maximum values of κ occur at locations near the wave peak (see Fig. 13), values of $\kappa_{\max}$ resemble those of $\hat{\kappa}$ from Fig. 11. Trends for the maximum gain, $\gamma_{\max}$, generally parallel those for $\kappa_{\max}$ in both the base and the apex. Note, however, that the ratio of the two makes a relatively abrupt transition at CFs near 3 kHz. (An apical-basal transition in the ratio $\gamma_{\max}/\kappa_{\max}$ is less apparent in the cat, although the data here are rather more sparse.) Because of this transition, the ratio $\gamma_{\max}/\kappa_{\max}$ is significantly larger in the base than in the apex.

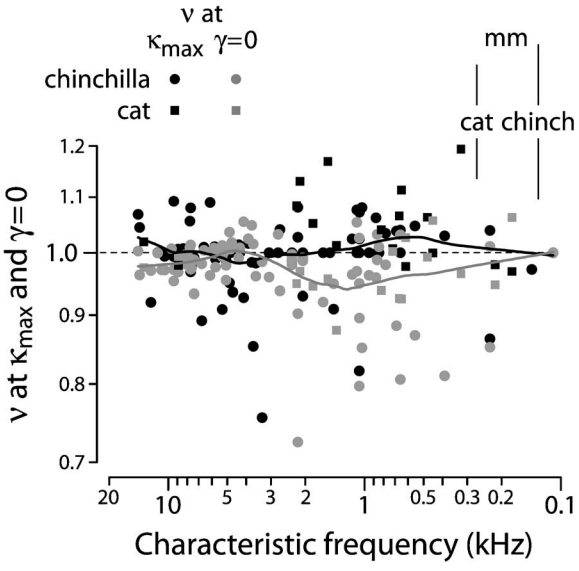

FIG. 13. Scatterplot of the maxima of $\kappa(\nu)$ and zeros of $\gamma(\nu)$ vs CF. Black symbols represent values of $\nu_{\kappa_{\max}}$ in chinchilla (circles) and cat (squares); gray symbols show values of $\nu_{\gamma=0}$. Solid lines show corresponding trends computed from the data pooled across species. For reference, a dashed line marks the wave peak ($\nu=1$). Scale bars of 1 mm are shown for use when interpreting the ordinate spatially.

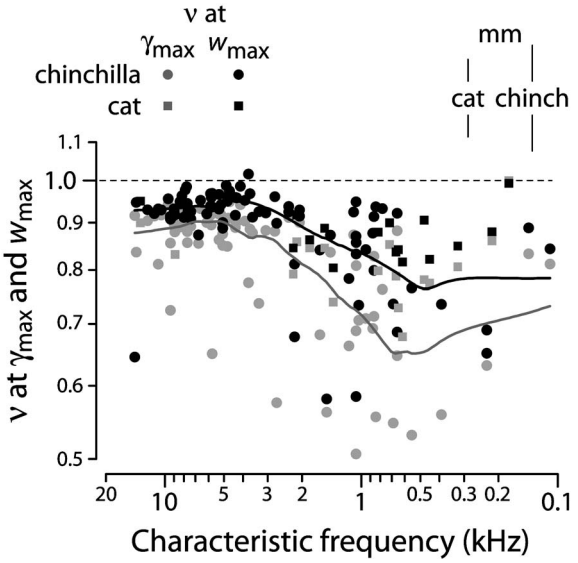

FIG. 14. Scatterplot of the maxima of $\gamma(\nu)$ and $w(\nu)$ vs CF. Gray symbols represent values of $\nu_{\gamma_{\max}}$ in chinchilla (circles) and cat (squares); black symbols show values of $\nu_{w_{\max}}$. Solid lines show corresponding trends computed from the data pooled across species. For reference, a dashed line marks the wave peak ($\nu=1$). Scale bars of 1 mm are shown for use when interpreting the ordinate spatially.

2. Locations of functional landmarks

Apical-basal differences are also evident in Figs. 13 and 14, which show scatterplots of the locations of functional landmarks of the propagation and gain functions. Figure 13 plots values of the scaling variable ν at locations where the propagation function $\kappa(\nu)$ reaches its maximum and where $\gamma(\nu)$ passes through 0 (i.e., where the power gain reverses sign). Both of these locations (denoted $\nu_{\kappa_{\max}}$ and $\nu_{\gamma=0}$, respectively) reside close to the wave peak ($\nu=1$) throughout the cochlea. Although $\nu_{\kappa_{\max}}$ and $\nu_{\gamma=0}$ appear nearly coincident in the base, the trend lines suggest that they separate slightly in the apex. In particular, the sign reversal in the gain function appears to occur somewhat basal to the peak ($\nu_{\gamma=0} < 1$) at CFs below about 3 kHz.

Figure 14 shows the locations of other features relevant to wave amplification. The gray symbols and trend line locate maximal values of the gain function γ, which occur everywhere basal to the wave peak. Whereas at high CFs the locations $\nu_{\gamma_{\max}}$ cluster about 0.9, at low CFs maximum values of γ occur further from the wave peak, at values averaging about 0.7. This decrease in the value of $\nu_{\gamma_{\max}}$ reflects the apical broadening of κ and γ evident in Figs. 8 and 9. Once again, the transition between apical and basal behavior occurs at CFs near 3 kHz. More functionally relevant than γ itself is the actual power transfer to the wave. The black symbols locate maximal values of $w(\nu)$, the per area power transfer given by Eq. (14). The trend indicates that maximal power transfer occurs closer to the wave peak than the maxima of γ. The apical-basal transition in the spatial extent of the gain region remains clearly apparent.

Although the derived gain functions provide estimates of the locations where the power gain peaks (namely, $\nu_{w_{\max}}$ or $\nu_{\gamma_{\max}}$ from Fig. 14) and estimates of where the gain region ends (namely, $\nu_{\gamma=0}$ from Fig. 13), the gain functions do not

provide especially reliable estimates of where the gain region actually begins. Although γ must first become positive somewhere basal to $\nu_{\gamma_{max}}$, and likely outside the peak region of the traveling wave, the dynamic range of the Wiener-kernel estimates of $V_{BM}(x_o,f)$ is too small to pinpoint the location. The higher dynamic range of the zwuis estimates renders them somewhat more informative in this regard, although the inversion procedure itself appears least accurate in the tail region of the response, where κ and γ are both small. These limitations notwithstanding, the gain functions shown in Fig. 10 indicate that in the apex the gain region extends for at least several millimeters basal to the peak.

Note that the data in Fig. 14 and elsewhere appear more variable below the apical-basal transition frequency than they do above. At least in part, the increased scatter reflects the larger spatial uncertainties associated with the broader propagation and gain functions characteristic of the apex (i.e., since broader functions are inherently less localized, their peak positions are more susceptible to noise).

3. Phase shifts and integrated power

The general decline in peak values of κ_{max} and γ_{max} observed during the progression from base to apex is accompanied by an increase in the width of the propagation and gain functions. This broadening is reflected in the basalward spread of the gain-function maximum at lower CFs ($\nu_{\gamma_{max}}$ in Fig. 14). In addition, reference to the Wiener-kernel transfer functions shown in Fig. 6 shows that the phase change across the peak is roughly constant in the base of the cochlea but increases in the apex. Approximate constancy in the base requires that the height and width of the peak in $\kappa(\nu)$ vary inversely in such a way that the area under the propagation function (i.e., the total phase change) remains roughly constant. At CFs below about 3 kHz, the propagation function broadens more rapidly than its height decreases (compare curves 4 and 5 in Fig. 9), and the phase shift across the (broader) peak region is therefore larger.

The gain functions show a similar pattern of variation along the cochlea, broadening while decreasing in peak amplitude in the base and then transitioning to a different behavior in the apex. To explore how these systematic changes in γ and κ affect the net power supplied to the wave, we integrate the power transfer per unit area, $w(x,f)$, along the cochlea, from the base to the point at which the power transfer reverses sign near the wave peak. More specifically, we compute[13]

$$\mathcal{P}_{\uparrow} = b\int_0^{x_0} w(x,f)dx, \tag{15}$$

where b is the effective BM width[14] and $x_0 \equiv x|_{\gamma=0}$ locates the downward zero-crossing of the gain function γ. The arrow on $\mathcal{P}_{\uparrow}$ indicates the direction of positive power transfer when the wave is pictured riding along on "top" of the organ of Corti—thus, $\mathcal{P}_{\uparrow} > 0$ implies power transfer from the organ of Corti down below to the wave up above. Before plotting, we divide the computed power by $\omega^3|\hat{D}_{BM}|^2 = \omega|\hat{V}_{BM}|^2$, where $|\hat{D}_{BM}| = |\hat{V}_{BM}|/\omega$ is peak BM displacement. Normalizing in this way removes changes in net power due simply to overall wave amplitude and frequency. We are asking, in effect, how the net power gain needed to produce the measured response would vary at different cochlear locations if the waves all had the same peak displacement and frequency. Although removing the dependence on peak displacement is mandated by the ANF-based data sets, which do not determine the absolute magnitude of V_{BM}, the normalization used here has the advantage of isolating only those contributions to the power gain that depend on the propagation and gain functions. (If desired, the effects of changes in wave frequency can be recovered by introducing an overall 18 dB/octave tilt.)

Figure 15 shows a scatterplot of the relative normalized power supplied to the wave ($\mathcal{P}_{\uparrow}/\omega^3|\hat{D}_{BM}|^2$) versus CF. The units along the ordinate are effectively dimensionless; they were chosen so that the trend approaches one at the highest CFs. The figure shows that the integrated contributions of κ and γ to the power gain of the cochlear amplifier are actually largest in the *apical* half of the cochlea and decrease systematically toward the base. The apical expansion of the spatial extent of the gain region evidently more than compensates for concomitant declines in γ_{max}.

D. Interdependence of κ and γ

Figure 16 demonstrates that the characteristic features of the propagation and gain functions described above are not independent of one another. In particular, the figure shows that $\kappa(\nu)$ and $\gamma(\nu)$ obey the so-called "Kramers–Krönig" dispersion relations (e.g., Kramers, 1927; Krönig, 1926; Zweig, 1976; Koshigoe and Tubis, 1982). Kramers–Krönig relations are nonlocal, integral equations that connect the real and imaginary parts of indices of refraction, scattering amplitudes, and other causal functions (e.g., Bode, 1945).[15] The dispersion relations for $\kappa(\nu)$ and $\gamma(\nu)$ have the form[16]

$$\kappa(\nu) = -\frac{2}{\pi}P\int_0^{\infty} \frac{\mu\gamma(\mu)}{\mu^2-\nu^2}d\mu, \tag{16}$$

and

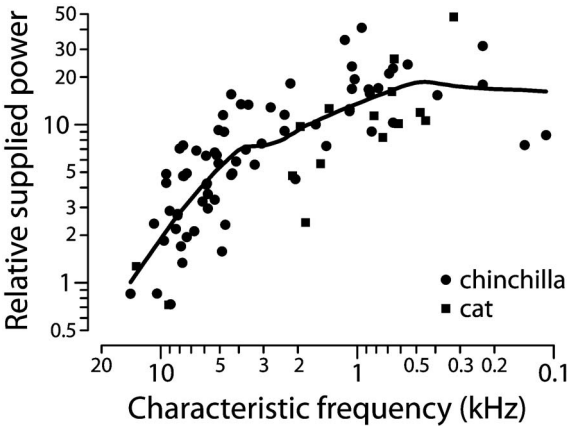

FIG. 15. Scatterplot of the relative power supplied to the wave ($\mathcal{P}_{\uparrow}/\omega^3|\hat{D}_{BM}|^2$) vs CF in chinchilla (circles) and cat (squares). Net power gains were computed using Eq. (15) and are shown in arbitrary units normalized so that the trend (solid line) is unity at the highest CF. The trend was computed from the pooled data.

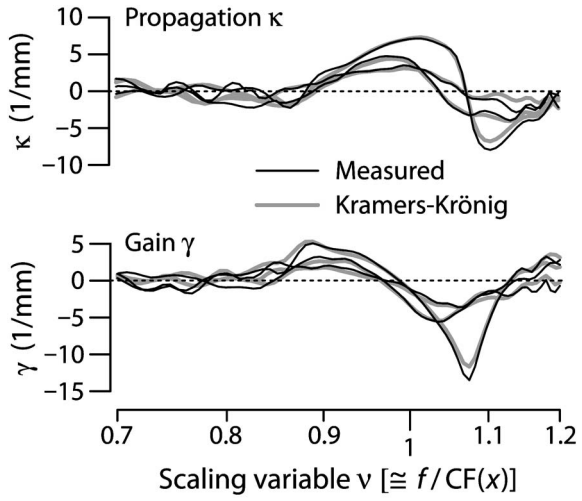

FIG. 16. Cochlear propagation and gain functions obey Kramers–Krönig dispersion relations. The figure shows empirical propagation and gains functions $\kappa(\nu)$ and $\gamma(\nu)$ derived from three example Wiener kernels with CFs near 9 kHz (thin black lines) along with their Kramers–Krönig counterparts computed one from the other (thick gray lines). The Kramers–Krönig $\kappa(\nu)$ in the top panel was computed from the empirical $\gamma(\nu)$ in the bottom panel using Eq. (16). The Kramers–Krönig $\gamma(\nu)$ in the bottom panel was computed from the empirical $\kappa(\nu)$ in the top panel using Eq. (17).

$$\gamma(\nu) = +\frac{2}{\pi} P \int_0^\infty \frac{\nu\kappa(\mu)}{\mu^2 - \nu^2} d\mu, \tag{17}$$

where the P before the integral denotes its Cauchy principal value (e.g., Mathews and Walker, 1964).[17] The figure shows derived propagation and gain functions for three example Wiener kernels along with corresponding functions obtained, one from the other, by evaluating Eqs. (16) and (17). The agreement is generally excellent in the peak region, where the propagation and gain functions are well determined. Matches of comparable or better quality, as assessed by computing the fractional rms error, were obtained for about 75% of the $\kappa(\nu)$ and $\gamma(\nu)$ pairs derived from the Wiener-kernel and zwuis responses (no systematic patterns were evident among the remainder). Evidently, the propagation and gain functions are mutually constrained by the Kramers–Krönig relations: The empirical form of $\kappa(\nu)$ determines that of $\gamma(\nu)$, and vice versa.

IV. DISCUSSION

A. Synopsis

Propagation and gain functions characterize the form and amplification of cochlear traveling waves. The properties of these functions, and their variation along the length of the cochlea, are central to an understanding of cochlear mechanics. We have presented a method for deriving propagation and gain functions from measurements of BM mechanical transfer functions. By applying the method to indirect estimates of near-threshold BM velocity obtained from: (1) Wiener-kernel analysis of chinchilla auditory-nerve responses to noise (Recio-Spinoso *et al.*, 2005) and (2) zwuis analysis of cat auditory-nerve responses to complex tones (van der Heijden and Joris, 2003, 2006), we derived propagation and gain functions throughout the cochlea in preparations uncompromised by surgical access to the scalae. In both species, and at all locations examined, the gain functions reveal a region of positive power gain basal to the wave peak. These results establish the existence of traveling-wave amplification throughout the cochlea, including the apex, where definitive conclusions have otherwise proved elusive.

Although qualitatively similar in form throughout the cochlea, the propagation and gain functions do manifest important quantitative variations with characteristic frequency. The catalog of basal to apical variations includes a systematic decline in the peak values of both κ and γ, as well as a concomitant increase in the spatial extent of the region of positive power gain. Unexpectedly, the integrated power gain attributable to the form of κ and γ appears largest in the apex rather than the base. The matching trends found in the behavior of the propagation and gain functions follow from the demonstration that the two functions are mutually constrained by the Kramers–Krönig dispersion relations.

Several properties of κ and γ undergo a relatively abrupt basal-apical transition at CFs of 3–4 kHz. (The data are more numerous and convincing in chinchilla, but a similar transition at similar CFs can also be discerned in the cat.) Interestingly, the CF location of the transition corresponds approximately with the frequency at which cat ANF tuning curves begin changing from the classic tip/tail form characteristic of high-CF fibers to the more complex, multilobed shapes found in the apex (Liberman, 1978; Liberman and Kiang, 1978). This CF also roughly corresponds to the location of a prominent bend in the frequency dependence of stimulus-frequency-emission delay in cat, guinea pig, and chinchilla (e.g., Shera and Guinan, 2003; Siegel *et al.*, 2005; Shera *et al.*, 2007). The origin and functional significance of these apparently correlated transitions between basal and apical-like behavior deserve further study.

B. Methodological and interpretive issues

1. Generality of the wave number

The model of cochlear hydrodynamics that underlies the wave number inversion procedure applies for short-, long-, and intermediate-wavelength traveling waves (Shera *et al.*, 2005). This generality plays an important role in the analysis, for although the long-wave approximation appears valid in the basal-most "tail" region of the cochlear response (e.g., Nedzelnitsky, 1980), the approximation breaks down near the peak, where the short-wave model is more appropriate. Validity of the long-wave approximation requires that the wavelength, λ, be large compared to the dimensions of the scalae. A rough guideline specifies that $2\pi H/\lambda < 1$, where H is the height (or radius) of the cochlear duct (e.g., Lighthill, 1981; de Boer, 1996). Figure 11 shows values of $\kappa H \equiv 2\pi H/\lambda$ for the chinchilla evaluated at the peak of the traveling wave using the derived propagation functions. The scatterplot demonstrates that except perhaps at the extreme apex of the cochlea, the hydrodynamics near the peak are everywhere short wave (see also van der Heijden and Joris, 2006).

Although the model supports both long and short waves, and waves of all lengths in between, the wave number inver-

sion formula derived in Sec. II B [Eq. (9)] implies that the propagation and gain functions are independent of the effective height (or width) of the scalae. In fact, they depend only on the given BM response function, $V_{BM}(x,f)$. In other words, any given mechanical response $V_{BM}(x,f)$ has unique propagation and gain functions irrespective of whether the hydrodynamics are long wave, short wave, or manifest a transition between the two, as in the real cochlea.

2. Consistency with inverse solutions for the BM impedance

The uniqueness of the propagation and gain functions that characterize a given BM mechanical response differs significantly from the situation surrounding the BM impedance and inversion procedures that can be used to find it. In contrast to the derived propagation and gain functions, the BM impedance necessary to produce a given $V_{BM}(x,f)$ depends strongly on the assumed nature of the hydrodynamics (Zweig, 1991; de Boer, 1995a; de Boer and Nuttall, 1999; Shera *et al.*, 2005). For example, although the BM impedances obtained using inversion procedures in long- and short-wave models have qualitative similarities (e.g., regions of negative resistance when employed on data from uncompromised preparations), they differ in important quantitative details, such as the locations of their "resonant" frequencies (zeroes of the reactance) and the strengths of the active forces.

To make these quantitative differences more explicit, we note that in short-wave models the BM impedance depends on the propagation and gain function through the relation

$$Z_{BM} = -(\gamma + i\kappa)|Z_f H/k^2| \quad \text{(short wave)}, \tag{18}$$

where Z_f is the effective acoustic impedance of the fluids [Eq. (7)]. In long-wave models, by contrast, the BM impedance has the value

$$Z_{BM} = -(2\gamma\kappa + i[\kappa^2 - \gamma^2])|Z_f/k^4| \quad \text{(long wave)}. \tag{19}$$

As these equations indicate, the real parts of both short- and long-wave BM impedances share a region of negative resistance where the gain function γ is positive (i.e., basal to the characteristic place) but have rather different magnitudes. As a result, the strength of the active forces necessary to produce a given BM velocity response differs considerably between the two models. The reactive components of the two BM impedances are even more dissimilar: Whereas the short-wave reactance remains stiffness dominated throughout the peak region (where $\kappa > 0$), the long-wave reactance has a zero (resonant frequency) at the point where $\kappa = -\gamma$, a condition satisfied at a location just apical to the response peak. These conclusions, deduced from Eqs. (18) and (19) and the qualitative forms of κ and γ described above, are consistent with inverse solutions for the BM impedance performed in 1D and 3D cochlear models (e.g., Zweig, 1991; de Boer, 1995a; de Boer and Nuttall, 1999).

3. Behavior beyond the best place

After decreasing from a maximum near the best place, the derived propagation functions often pass through zero and become negative at more apical locations (cf. Fig. 7). Simply interpreted, negative values of κ suggest that waves are traveling backward toward the stapes. However, the decrease in κ and the appearance of negative values in this region actually reflect the transition from propagating to evanescent (nonpropagating) wave behavior characteristic of the "cutoff" region beyond the wave peak. Wave propagation requires the dynamical interplay of the kinetic energy of fluid motion and the potential energy of partition stiffness. In the cutoff region, however, the reactive component of the BM impedance is controlled not by the partition stiffness, but by its mass (e.g., de La Rochefoucauld and Olson, 2007). Note, for example, that negative values of κ yield a positive (i.e., mass-dominated) BM reactance when substituted into the short-wave expression for Z_{BM} [Eq. (18)]. As a result, wave propagation cannot occur in this region, and the straightforward interpretation of the sign of κ no longer applies.

When combined with local scaling, the decline in the propagation function apical to the best place predicts a corresponding decrease in the wave group delay. The group delay τ_{grp} is defined by

$$\tau_{grp} \equiv -\frac{1}{2\pi}\frac{\partial\varphi}{\partial f} \cong -\frac{1}{2\pi}\frac{\partial}{\partial f}\int_0^x \kappa(x',f)dx', \tag{20}$$

where $\varphi(x,f)$ is the wave phase, and the approximation neglects small contributions from the $k^{3/2}$ prefactor in Eq. (11). Local scaling implies that the spatial integral and its frequency derivative can both be reexpressed in terms of ν. In particular, $dx = (\partial x/\partial\nu)d\nu$ and $\partial/\partial f = (\partial\nu/\partial f)\partial/\partial\nu$, where the necessary partials can be computed from Eq. (5). Evaluating Eq. (20) then yields

$$\tau_{grp}(\nu,f) \cong \frac{l}{2\pi(f + \mathrm{CF}_1)}\kappa(\nu), \tag{21}$$

where l and CF_1 are parameters of the cochlear map [Eq. (4)]. At fixed frequency, Eq. (21) predicts that the wave group delay manifests the same qualitative behavior as $\kappa(\nu)$. Specifically, the analysis predicts that measured group delays increase to a maximum near the best place and decrease beyond. This paradoxical (because seemingly acausal) decrease in the group delay at more distant locations results from the transition to evanescent behavior.[18]

4. Local scaling and other approximations

Although the inversion procedure does not itself rely on local scaling (Sec. II B), the transformation applied here to convert measured frequency-domain transfer functions (e.g., Wiener kernels) into the traveling waves needed as raw material for the inversion does assume this approximate symmetry (Sec. II A). Although significant deviations from scaling become apparent when cochlear responses are compared across one or two octaves of CF (Fig. 6; see also Shera and Guinan, 2003), the conversion used here requires only that the symmetry apply over distances corresponding to the width of the transfer function peak. (The dynamic range of the Wiener kernels is generally insufficient to provide useful information outside the peak region. Fortunately for our purposes, most of the amplification and dispersion occurs near

the peak.) Except perhaps at the extreme apex of the cochlea, where transfer functions can span several octaves, the local scaling approximation appears well satisfied.

Direct measurements of the traveling wave performed using scanning interferometry (Ren, 2002) corroborate the validity of local scaling in the base of the cochlea. To wit, Ren's gerbil traveling waves and transfer functions, although measured in different preparations, nearly overlie one another when plotted using the scaling variables β or ν. As an additional check on the validity of local scaling, we applied the inversion procedure directly to Ren's traveling waves, for which no scaling assumptions are needed, and obtained propagation and gain functions with the same qualitative features that emerge from the analysis of the Wiener-kernel and zwuis transfer functions in the chinchilla and cat. In addition, the inversion procedure yields values of κ that agree well with those obtained by direct spatial computation of the real part of the wave number in gerbil (de La Rochefoucauld and Olson, 2007).

In the apex, van der Heijden and Joris (2006) confirm the violation of traditional scaling expected from changes in the shapes of cat neural tuning curves (e.g., Kiang and Moxon, 1974; Liberman, 1978). Deviations from traditional scaling can be substantially reduced, although not eliminated, by means of the generalized local scaling introduced here. Although quantitative details, such as the values of $\hat{\kappa}$ shown in Fig. 11, depend on to the choice of scaling variable (ν versus β), qualitative features of the propagation and gain functions, such as the existence of power gain basal to the wave peak, are quite robust. Although we expect residual violations of generalized scaling to introduce systematic errors, it is reassuring to note that the values of κ we obtained in cat are consistent with estimates of the wavelength obtained from "panoramic" (i.e., spatial) profiles of cochlear phase constructed from the same data by van der Heijden and Joris (2006).[19] Thus, the consistency of our results with independent estimates of the wavelength from both the base and the apex suggests that our findings are unlikely to be artifacts introduced by the local scaling approximation.

Since we obtained similar results when analyzing direct mechanical measurements (e.g., Ren, 2002; de La Rochefoucauld and Olson, 2007), neither are our findings a consequence of employing Wiener-kernel or zwuis-based estimates of BM velocity responses. The Wiener-kernel and similar measurements characterize the traveling wave as seen from the auditory nerve. In principle, they therefore include contributions from internal motions of the organ of Corti that may be visible to the inner hair cell but appear less prominent in the motion of the BM (e.g., Guinan *et al.*, 2005; Nowotny and Gummer, 2006; Karavitaki and Mountain, 2007). Although subtle systematic differences will doubtless be discovered, Wiener-kernel responses corrected for synaptic and neural transmission delays closely resemble BM mechanical measurements made at corresponding locations and intensities (Temchin *et al.*, 2005).

5. When things fall apart

The major limitation of the wave number inversion procedure is that it doesn't always work when applied to real data. In a significant minority of cases the inversion produces a reconstructed $V_{\mathrm{BM}}(x,f)$ with sharp spikes or discontinuities not present in the original. [Like the little girl with the curl (Longfellow, 1922), when the reconstructions are good, they are very good indeed, but when they are bad, they are horrid.] Anomalies and other problems were present even in regions where the estimated BM response appeared well determined; they were especially common in the "cutoff" region apical to the best place (or at frequencies above CF). Tests of the inversion procedure using model-generated responses for which the actual wave number is known suggest that poor reconstructions can result from errors in the assumed boundary conditions and/or from contamination by higher-order, nonpropagating (evanescent) modes. They may also result from inaccuracies in the Wiener-kernel or zwuis estimates of BM motion. Interestingly in this regard, the overall failure rate of about 30%–40% masks a significant dependence on CF: the probability of obtaining an unsuccessful reconstruction was roughly twice as large for CFs above 3 kHz than it was below (0.45 versus 0.21). However, similar reconstruction problems were also encountered when analyzing BM mechanical measurements obtained using laser vibrometry. The invention of methods to mitigate or eliminate these problems would improve the reliability, and presumably also the accuracy, of the procedure. The trends and conclusions reported here are based on cases validated by successful reconstruction. This restriction was imposed more for logical consistency than for practical necessity; including errant wave numbers in the analysis increased the amount of scatter but did not alter the overall trends (e.g., in Figs. 11–15).

6. Estimating the power gain of the cochlear amplifier

In principle, the propagation and gain functions can be used to find the power gain of the cochlear amplifier.[20] Energy conservation requires that the total power entering the cochlea at the stapes ($\mathcal{P}_{\Rightarrow}$) equal the power absorbed within the cochlea ($\mathcal{P}_{\Downarrow}$) plus any power reemitted ($\mathcal{P}_{\Leftarrow}$). In other words,

$$\mathcal{P}_{\Rightarrow} = \mathcal{P}_{\Downarrow} + \mathcal{P}_{\Leftarrow} \cong \mathcal{P}_{\Downarrow}, \tag{22}$$

where the approximation is valid when the reemitted power (e.g., stimulus-frequency emission) is small compared to the stimulus.[21] As discussed in Sec. III C 3, the absorbed power can be computed from the integral

$$\mathcal{P}_{\Downarrow} = -b\int_0^L w(x,f)dx, \tag{23}$$

where $-w(x,f)$ is the power per unit BM area dissipated within the organ of Corti. By splitting the integral into two parts, Eq. (23) can be written in the form

$$\mathcal{P}_{\Downarrow} = -\mathcal{P}_{\uparrow} + \mathcal{P}_{\downarrow}, \tag{24}$$

where

$$\mathcal{P}_{\uparrow} \equiv b\int_0^{x_0} w\,dx \text{ and } \mathcal{P}_{\downarrow} \equiv -b\int_{x_0}^{L} w dx. \tag{25}$$

Introduced in Eq. (15), $\mathcal{P}_{\uparrow}$ represents the net power transfer

to the wave in the region basal to x_0; $\mathcal{P}_\downarrow$ is the net power absorbed *from* the wave in the region apical to x_0. Figure 13 shows that x_0 is nearly coincident with or slightly basal to the wave peak.

A physically relevant measure of the net power gain of the cochlear amplifier can now be obtained by computing the ratio

$$G \equiv \frac{\mathcal{P}_\Rightarrow + \mathcal{P}_\uparrow}{\mathcal{P}_\Rightarrow} = 1 + \frac{\mathcal{P}_\uparrow}{\mathcal{P}_\Rightarrow}. \tag{26}$$

Equivalent to the metric adopted by de Boer and Nuttall (2001), the power gain G is just the total forward power at x_0 normalized by the power input at the stapes. Since the total power is the input power plus the net power supplied to the wave, G is greater than one when the organ of Corti provides net power gain ($\mathcal{P}_\uparrow > 0$) and less than one when there is net power loss ($\mathcal{P}_\uparrow < 0$), as in a passive preparation. Note, however, that because G measures only the *net* power gain, it underestimates the *total* power supplied to the wave by the organ of Corti, some of which necessarily goes toward compensating for passive losses. Unless the total power supplied exceeds these losses, the net gain G will remain less than one.[22]

Equation (26) can be simplified by combining Eqs. (22) and (24) to yield $\mathcal{P}_\Rightarrow \cong \mathcal{P}_\downarrow - \mathcal{P}_\uparrow$. Consequently,

$$G \cong \frac{1}{1 - \mathcal{P}_\uparrow/\mathcal{P}_\downarrow}, \tag{27}$$

a quantity that can be computed from the derived propagation and gain functions. Note that the gain G is independent of any factors common to both $\mathcal{P}_\uparrow$ and $\mathcal{P}_\downarrow$ that divide out in their ratio (e.g., the BM width and the unknown overall wave amplitude, $\hat{V}_{\mathrm{bm}}$). Unfortunately, Eq. (27) also implies that accurate estimates of G are likely unattainable from experimental data in individual animals, at least when the gain is large. Large values of G occur when the ratio $r \equiv \mathcal{P}_\uparrow/\mathcal{P}_\downarrow$ is close to one, where $G(r)$ is singular. Since they depend on the small difference between two larger numbers, large values of G are therefore especially susceptible to error. Indeed, since $\Delta G = G^2 \Delta r$, uncertainties Δr are boosted by the factor G^2 and increase faster than the gain itself. Thus, as the power gain becomes large, errors in computing r appear magnified, sometimes enormously, in G.

Figure 17 shows empirical values $r \equiv \mathcal{P}_\uparrow/\mathcal{P}_\downarrow$ representing ratios of net power supplied to/delivered by the wave. Although r declines somewhat at the highest CFs, the values generally cluster near $r=1$, indicating substantial power gains throughout the cochlea. In particular, r appears large even in the apex (indeed, perhaps especially in the apex). Note that values $r \geqslant 1$ are forbidden by energy conservation if $\mathcal{P}_\Leftarrow = 0$. Empirical ratios r at values greater than 1 must thus reflect violations of the no-emission approximation[23] and/or errors due to the finite precision of the data and their analysis. Collapsing the estimates across CF yields a median r of 0.95 and a mean of 0.94 ± 0.07, with uncertainties representing approximate 95% confidence intervals. The confidence intervals for r correspond to net power gains spanning the range $G \in [7, \infty]$, with a mean of approximately 17. (When expressed in dB, computed as $10 \log G$, the corresponding gain range is $[8, \infty]$ dB, with a mean near 12 dB.) Of course, the semi-infinite uncertainty on the estimate of G provides an important caveat. Were it to prove representative of actual cochlear power gains, the value $r=0.94$ would imply that at least 94% of the wave power reaching its characteristic place originates *within* the cochlea.

Both our rough estimate of the mean power gain and its substantial uncertainty (as well as the large apparent variability in gain between individuals) are consistent with results reported by de Boer and Nuttall (2001). Based on an inverse analysis of data from 20 good preparations, they report net gains in guinea pig ranging from 0.2 to 17.7 dB computed using an equivalent metric. Our analysis shows that much if not all of the variability in estimates of the net power gain arises through the error magnification inherent in Eq. (27) for G at large gains. Although experimental uncertainties and their magnification preclude precise quantification of the power gain from the data employed here, our results do demonstrate significant gain throughout the cochlea.

C. Interpretation as a hydromechanical laser amplifier

The empirical cochlear propagation and gain functions obtained here resemble those that characterize electromagnetic wave propagation in an active optical gain medium. Indeed, our results corroborate previous suggestions (Zweig, 1991; Russell and Kössl, 1999; Kemp, 2002; Shera, 2003a) by demonstrating that the cochlea functions as a biological analog of a laser amplifier.

An optical laser amplifier consists of a "gain medium" that supports electromagnetic wave propagation, perhaps a gas or crystal, and a power supply or pumping process that puts the atoms of the medium into an excited state [see Fig. 18(A)]. When the atoms relax they spontaneously emit incoherent light—light, that is, with a mix of directions, phases, and polarizations. But when light from an external source illuminates the medium, it stimulates the atoms to radiate in phase with the input, producing a like-upon-like coalescence

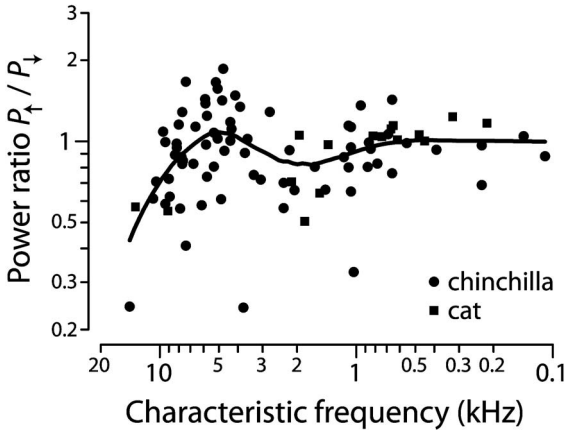

FIG. 17. Scatterplot of $r \equiv \mathcal{P}_\uparrow/\mathcal{P}_\downarrow$ vs CF in chinchilla (circles) and cat (squares). Computed using Eq. (25), r is the ratio of the net powers supplied to/delivered by the wave in regions basal/apical to the point (x_o) where the power flow reverses near the peak of the wave. The trend (solid line) was computed from the pooled data and indicates that r is fairly close to one, implying the existence of substantial power gains throughout the cochlea.

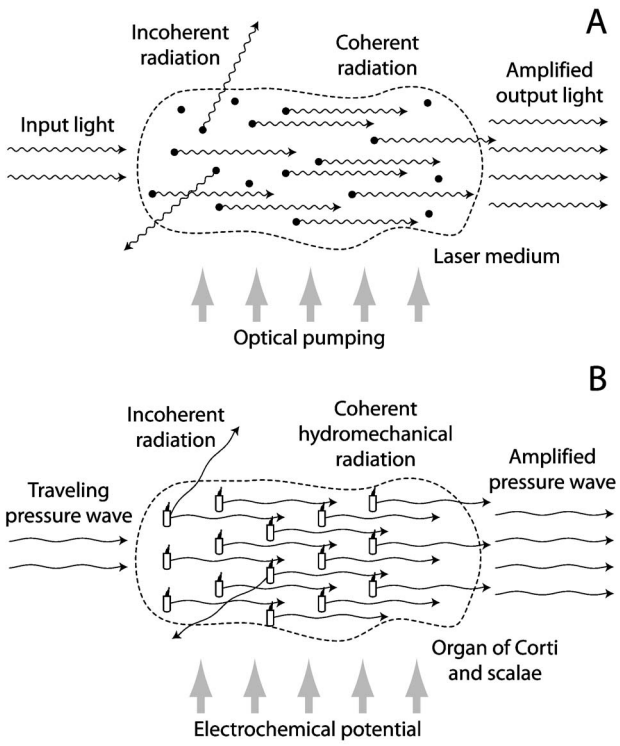

FIG. 18. Analogy between laser and cochlear amplifiers. The top panel (A) shows the essentials of a laser amplifier. When excited by an optical pumping process, atoms embedded in a gain medium that supports electromagnetic wave propagation spontaneously emit incoherent light. Light of the same frequency applied at the input stimulates the atoms to radiate in phase, amplifying the applied beam. The bottom panel (B) shows corresponding features of the cochlear amplifier. When stimulated via bundle displacements induced by the traveling pressure-difference wave, hair cells create forces that couple to their mechanical environment, producing hydromechanical radiation that combines coherently with and amplifies the incident pressure wave. Although each cell may radiate symmetrically in both directions, the backward radiation combines incoherently and tends to cancel out (Shera, 2003b; Shera and Guinan, 2007); only the forward radiation is shown here. Brownian motion also drives the individual hair bundles, resulting in incoherent hydromechanical radiation whose amplitude and phase differ from cell to cell. (For the purposes of illustration, this incoherent radiation is shown propagating obliquely.) The amplification process is powered by the electrochemical potentials that drive ionic currents through the hair-cell transduction channels.

of external and stimulated radiation. The result is an amplified output beam: The power in the signal beam is boosted by coherent amplification. The process of stimulated emission and amplification occur when the frequency of the incident light closely matches the frequency of the radiation emitted by the atoms of the gain medium, a frequency determined by atomic energy levels, in particular by the quantized energy difference between the excited and relaxed states (for an excellent review see Siegman, 1986).

The propagation and gain functions derived here indicate that when stimulated by a passing wave, the cochlear gain medium "emits" hydromechanical radiation that combines coherently with and boosts the amplitude of the incident wave ($\gamma > 0$) in a region basal to the characteristic place (see also Zweig, 1991). Although many details of the biophysical workings of the gain medium remain uncertain, the cochlear analogues of major functional elements of the optical laser are clear [see Fig. 18(B)]. In the cochlea, traveling-wave amplification is hydromechanical rather than electromagnetic and quantum mechanical. The disturbances that propagate in the medium are cochlear traveling pressure-difference waves rather than light. The gain medium responsible for coherent wave amplification consists not of excited atoms but of the cellular force generators and concomitant mechanical, hydrodynamic, and electrical processes known collectively as the "cochlear amplifier" (Neely, 1983). The power supply, or battery, is the electrochemical gradient that drives ionic currents through the hair cells, changing their receptor potentials and inducing conformational changes in transmembrane proteins. These conformational changes exert forces that are transmitted through the organ of Corti via its elaborate cytoarchitectural scaffolding. Ultimately (and herein much of the mystery lies), these forces create pressure gradients in the surrounding fluids that, according to the present analysis, combine coherently with the stimulus wave to boost the amplitude of the response.

1. An analytic twist

Unlike a conventional laser amplifier, the cochlea has functional requirements more fundamental than providing power gain. First, the cochlea must *analyze* the signal it amplifies. Although the beam directed to an optical amplifier simply passes through the medium for a boost on its way to other things, the sound input to the cochlea must be separated into frequency components and directed onto different populations of sensory cells embedded within the gain medium itself. Immediately thereafter, the wave excitation must be rapidly extinguished to minimize interference with the analysis of ongoing sounds. Second, cochlear operation must be *wideband*: Although a conventional optical amplifier operates only within the extremely narrow frequency range determined by the atomic transition, the cochlea must cope with any sound within the frequency range of hearing. Accommodating these basic requirements for wideband analysis and amplification requires a crucial modification to the propagation and gain functions found in a conventional laser medium.

In an idealized optical gain medium the wave number k_{optical} has the form

$$k_{\text{optical}} = \kappa_0 + k_{\text{laser}}, \tag{28}$$

where $\kappa_0 = \omega/c$ and c is the speed of light in the host medium. (Ohmic losses are usually small and have been neglected for simplicity.) The interesting action occurs in k_{laser}, which characterizes the atomic contribution to the wave number due to amplifying interactions within the medium. The real and imaginary parts of k_{laser} represent the laser propagation and gain functions:

$$k_{\text{laser}} = \kappa_{\text{laser}} + i\gamma_{\text{laser}}. \tag{29}$$

The top panel of Fig. 19 illustrates the qualitative behavior of κ_{laser} and γ_{laser} at frequencies in the immediate neighborhood of the atomic transition frequency, f_{atomic}. The laser gain function is positive ($\gamma_{\text{laser}} > 0$) but vanishingly small everywhere except in a narrow band near the frequency f_{atomic}, about which it manifests a symmetric Lorentzian resonance characteristic. By contrast, the laser propagation function is

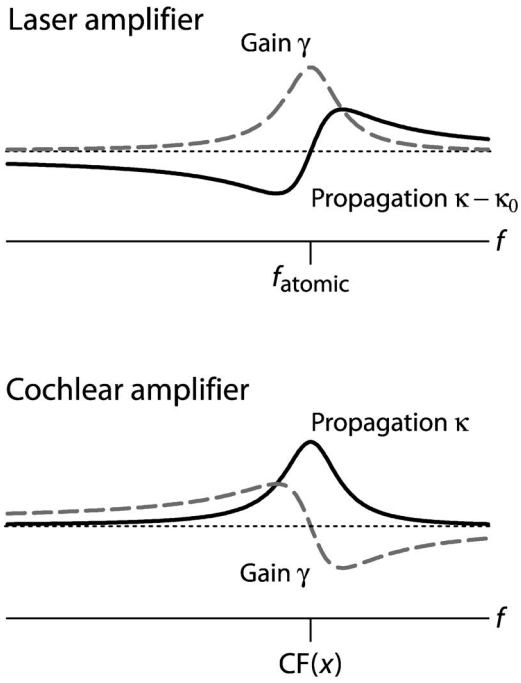

FIG. 19. Propagation and gain functions for laser and cochlear amplifiers versus frequency. The top panel shows stylized propagation and gain functions for an optical laser amplifier in the frequency region about the atomic transition frequency, f_{atomic}. Only the resonant, atomic contribution to the laser propagation function is shown; the constant wave number κ_0 corresponding to background propagation in the host medium has been subtracted off. [Adapted from Figs. 2.8 and 7.3 of Siegman (1986).] The bottom panel shows stylized versions of the empirical cochlear propagation and gain functions derived here (see Figs. 8 and 9). The cochlear wave number appears isomorphic to the laser wave number rotated 90° clockwise in the complex plane. In both panels, dotted lines mark the zero along the ordinate. Note that the laser functions are substantially narrower than those in the cochlea. Had they been drawn on the same logarithmic axis used for the cochlea, the laser functions would have bandwidths smaller than the dots that compose the zero lines. In the cochlea, local scaling can be used to convert the frequency axis into a spatial one. The clockwise twist shown here is crucial to the operation of the cochlea, which must also analyze the signals it amplifies. Useful analysis requires both level-dependent amplification (to match the variance of the incoming signal to the dynamic range of the detectors) and attenuation (to clear the stage for the analysis of future sounds). The result is a region with $\gamma > 0$ followed by one with $\gamma < 0$.

antisymmetric about f_{atomic}. At frequencies below the atomic transition frequency ($f < f_{\text{atomic}}$), the propagation function is negative ($\kappa_{\text{laser}} < 0$), and the effective propagation coefficient ($\kappa_0 + \kappa_{\text{laser}}$) is therefore smaller than κ_0. At these frequencies, amplifying interactions with the gain medium therefore increase the wavelength and velocity of the light wave through the medium; at frequencies above the transition, the same interactions decrease them. The differing behaviors of κ_{laser} and γ_{laser} are mutually interdetermined through the Kramers–Krönig dispersion relations.

The overall "shapes" of the cochlear propagation and gain functions derived here resemble those of an optical medium, but with the crucial twist that the roles played by κ_{laser} and γ_{laser} are interchanged. More precisely, they are rotated in the complex plane in a way that preserves the Kramers–Krönig relations. In particular,

$$k_{\text{cochlea}} \sim -ik_{\text{laser}}, \tag{30}$$

where the tilde signifies the overall isomorphism and the subscript "cochlea" has been added for clarity. (Any cochlear analogue of the wave number κ_0 appears small.) The $-i$ multiplying the laser wave number rotates its components clockwise through one quarter cycle, effectively switching the roles of propagation and gain functions:

$$\kappa_{\text{cochlea}} \sim \gamma_{\text{laser}} \tag{31}$$

and

$$\gamma_{\text{cochlea}} \sim -\kappa_{\text{laser}}. \tag{32}$$

For comparison with their laser counterparts illustrated in the top panel, the bottom panel of Fig. 19 shows stylized versions of the cochlear propagation and gain functions derived from experiment (cf. Figs. 8 and 9). In the cochlea, the role of the atomic transition frequency is played by CF(x), which varies with location within the medium. Although the relative scales were chosen to emphasize the isomorphism of shape, the fractional bandwidths of the curves about their center frequencies [e.g., the width of γ_{laser} about f_{atomic} and of κ_{cochlea} about CF(x)] are much smaller (narrower) for the optical laser than they are in the cochlea. In optical lasers, relative bandwidths are often considerably less than fractions of a percent;[24] in the cochlea, they are at least 10% in the base and can be significantly greater in the apex (see Fig. 9).

Because of the effective rotation of the wave number, the cochlear gain medium—unlike the laser medium—is strongly dispersive. Whereas light amplified by a laser undergoes negligible change in wavelength or velocity as it propagates through the medium [$\kappa_{\text{laser}}/\kappa_0 \ll 1$ with $\kappa_{\text{laser}}(f_{\text{atomic}}) \cong 0$], the cochlear propagation function resembles the laser gain function and depends strongly on frequency. Because of local scaling, frequency dispersion is equivalent to spatial dispersion: The wavelength and velocity of the cochlear traveling wave therefore depend strongly on position, and the wave slows considerably as it approaches its characteristic place. The cochlear gain function mirrors the antisymmetric laser propagation function. Unlike an optical laser, where maximum gain occurs at the frequency f_{atomic}, the maximal value of γ_{cochlea} occurs at frequencies below CF(x). At frequencies above CF(x) the gain function reverses sign, and waves are strongly squelched. Again, local scaling converts this frequency variation into a spatial pattern in the cochlea—traveling waves are amplified as they approach their characteristic place and strongly attenuated beyond. Thus, in contrast to an optical laser, where amplification occurs uniformly throughout the medium, amplification in the cochlea is spatially localized.

Thus, the strong dispersion and concomitant absorption introduced by rotating the laser wave number and varying CF(x) with position allow the cochlear gain medium to perform both wideband amplification and analysis. Although each section of the cochlea amplifies a limited range of frequencies—according to the cochlear gain functions shown in Fig. 9 this range extends in the chinchilla from roughly one third of an octave below CF in the base of the cochlea to as much as an octave below CF in the apex—together they amplify any frequency for which vibration of the stapes launches a traveling wave. In principle, wideband amplification—but not analysis—could be achieved using conventional laser gain functions; for example, by construct-

ing the gain medium from a mixture of atoms with a wide array of transition frequencies. But useful analysis requires both strong dispersion, to separate signals into their component frequencies, and regions of *negative* power gain, so that amplified signal energy, once transduced, will be reabsorbed within the medium rather than be allowed to linger, compromising the analysis of future sounds.

2. Emergence of laser oscillations

Our results demonstrating laser-like *amplification* within the mammalian cochlea corroborate earlier findings of laser-like *oscillations* emitted from the ear (Kemp, 1979; Shera, 2003a). An optical laser amplifier can be transformed into a laser oscillator—a device that *generates* light rather than simply amplifying it—by embedding the gain medium in a resonant cavity; for example, by adding mirrors at the boundaries to reflect light back through the medium, creating a feedback loop that recycles the output back to the input. If the size of the cavity is tuned just right, so that the round-trip distance encompasses an integral number of wavelengths of the emitted light, then standing waves can build up inside the cavity. The amplitude of these standing waves is determined by the round-trip power gains and losses. If one of the mirrors is made partially transparent, the system will emit a beam of coherent light—a laser beam.

The cochlea, too, contains mirrors. In the cochlea, the "resonant cavity" spans the region between the stapes and the peak of the traveling wave. At either end of this region, cochlear traveling waves are partially reflected back into the cavity. At the apical end of the cavity, forward-traveling waves are partially reflected (or reemitted) through the process that generates stimulus-frequency otoacoustic emissions [e.g., coherent reflection off mechanical "imperfections" in the gain medium near the peak of the traveling wave (Zweig and Shera, 1995; Talmadge *et al.*, 1998; Shera *et al.*, 2005)]; at the stapes, backward-traveling waves reflect due to the impedance mismatch with the middle ear (Shera and Zweig, 1991; Puria, 2003).[25]

On each pass through the cavity, cochlear traveling waves are amplified by their interaction with the gain medium. At certain special frequencies—those for which the round-trip phase change is an integral number of cycles—multiple internal reflection creates standing waves. If the round-trip gain matches the round-trip losses (e.g., due to damping and acoustic radiation into the environment), stable oscillations can result that appear in the ear canal as spontaneous otoacoustic emissions (SOAEs). Unlike optical oscillators, the cochlea can emit at multiple, nonharmonically related frequencies. In an optical laser, the cavity size is fixed and tuned to a single frequency and its harmonics. Wave propagation in the cochlea, however, is highly dispersive and the location of the wave peak—and hence the location of the partially reflecting mirror—depends on frequency. Consequently, the round-trip phase condition is satisfied at many frequencies and the cochlea can—and does—produce multiple SOAEs simultaneously.

Just as in an optical laser, oscillation amplitudes are self-stabilizing. Since the cochlear gain medium is limited in the energy it can produce, amplification is nonlinear (amplitude dependent), decreasing as the wave amplitude grows. Standing-wave amplitudes are therefore stable against perturbations: If some random fluctuation increases the wave amplitude slightly, the round-trip gain decreases a little and the wave amplitude falls back down. Conversely, if the wave amplitude decreases, the total gain increases, pulling the oscillation amplitude back up. Amplitude stabilization of this sort produces acoustic SOAE signals with statistical properties identical to those that characterize the coherent electromagnetic radiation generated by optical lasers (e.g., Golay, 1961; Siegman, 1986; Shera, 2003a).

3. Meaning of the dispersion relations

In optical lasers and other physical systems, adherence to Kramers–Krönig dispersion relations is generally a consequence of causality (e.g., Toll, 1956). Causality requires that a system not respond before it is driven. Although causality is thought to constrain all physical interactions, its application to the propagation and gain functions derived here arises not as the universal and inevitable consequence of fundamental physics but reflects the detailed and contingent dynamics of the cochlea. According to Eqs. (6) and (7), k^2 can be written in the form

$$k^2 = -bZ_f V_{BM}/\bar{P}. \tag{33}$$

In this equation, k^2 plays a role analogous to an admittance, characterizing the system's response (V_{BM}) to an impressed force ($\bar{P}$). Thus, the approximate empirical adherence to the Kramers–Krönig relations demonstrated in Fig. 16 reflects the approximate causality of the BM response to $\bar{P}$.

The approximate causality implied by the Kramers–Krönig relations is dynamically significant because $\bar{P}$ is not necessarily the only force acting upon the BM. (In fact, because $\bar{P}$ is the pressure difference averaged in the "vertical" direction above the BM, the pressure $\bar{P}$ is not physically driving the BM at all.) In principle, the motion of the BM could—and at some level must—be driven by forces communicated from nearby locations by means other than scalae-fluid pressure. Possible alternate routes include "feed-forward" mechanisms such as the longitudinal tilt of the outer hair cells (e.g., Kolston *et al.*, 1989; Steele *et al.*, 1993; Geisler and Sang, 1995), fluid flow in the tunnel of Corti (Karavitaki and Mountain, 2007), or subtectorial space (Nowotny and Gummer, 2006), mechanical and electrical coupling within the organ of Corti (reviewed in Santos-Sacchi, 2000) or along the tectorial membrane (Ghaffari *et al.*, 2007), as well as neural interactions among the outer hair cells (e.g., Thiers *et al.*, 2002). When timed appropriately, "nonclassical" forces such as these can give rise to both noncausal point-impedance functions (de Boer, 1997a) and noncausal values of k^2. The fact, however, that the empirical adherence to the Kramers–Krönig relations appears as good as it does indicates that any noncausal contributions to BM propagation and amplification (i.e., forces fed forward relative to $\bar{P}$) must be relatively small, at least in their effect on the wave peak.

4. Interrelationship of propagation and gain

The propagation and gain functions determined here describe qualitatively different phenomena in the cochlea. Whereas $\kappa(x,f)$ characterizes traveling-wave dispersion, $\gamma(x,f)$ describes power amplification and absorption. Direct measurement of one would require equipment and analysis ill suited to measurement of the other. Despite these *qualitative* differences, cochlear propagation and gain functions appear *quantitatively* related: The Kramers–Krönig relations satisfied by $\kappa(x,f)$ and $\gamma(x,f)$ [Eqs. (16) and (17)] imply that the form of one determines the form of the other. Thus, the properties of cochlear amplification (e.g., gains and spatial distributions) cannot be changed without simultaneously changing the characteristics of wave propagation (e.g., wavelengths, velocities, and delays), and vice versa (see also Zweig, 1976; de Boer, 1997b). In the cochlea, propagation and gain are inseparably complected aspects of the same process: In a deep way, made precise by Eqs. (16) and (17), the wavelength of the traveling wave *is* the amplifier.

5. Biophysics of the gain medium

By stripping away uncertainty about the biophysical underpinnings to reveal the basic functional operation of the cochlea—a wideband, hydromechanical laser analyzer—the present analysis emphasizes a point often obscured by molecular detail: Cochlear traveling-wave amplification is distributed and involves coupling among elements over a relatively broad region of the cochlea. According to the results from Fig. 8, this region is at least 1 mm in the base and several times that in the apex (1 mm comprises approximately $3\times100=300$ outer hair cells). In the base of the cochlea, this lower bound on the spatial extent of power amplification is consistent with indirect estimates in guinea pig derived either from acoustic-lesion studies (Cody, 1992) or from manifestations of mechanical nonlinearity (Russell and Nilsen, 1997).

Although it is sometimes implied that outer hair cells or their components—their soma, their bundles, even individual proteins—are by themselves responsible for traveling-wave amplification, the cochlear amplifier is an emergent property of collections of cells coupled together by mechanical, electrical, and hydrodynamic interactions. As a result, there can be no simple relation between the forces produced by isolated hair cells, or by the proteins expressed within them, and the gain or other functional characteristics of the cochlear amplifier. Indeed, identical hair cells placed in different hydromechanical environments (e.g., in scalae of different heights) can produce dramatically different BM response functions (Shera *et al.*, 2005). Implicit in most models of cochlear mechanics, these observations warrant emphasis here only to remind ourselves that the obvious is easily overlooked (e.g., Poe, 1844).

As reviewed above, the propagation and gain functions depend only on BM velocity; they are robust to changes in the effective dimensionality of cochlear hydrodynamics. In a similar way, they place few specific constraints on the biophysical mechanisms involved in realizing the cochlear amplifier. Just as one can construct functioning optical lasers around a variety of gain media, so from the perspective of the cochlear propagation and gain functions, many details of organ of Corti micro- and nanomechanics remain shielded from view. A variety of different impedance and coupling combinations can combine to produce similar, even identical, response functions, and thereby yield similar propagation and gain functions.

The problem of understanding the biophysics of the gain medium must therefore be tackled simultaneously both from above and from below. Because the amplifier involves cooperation and coupling among many components, it will never be understood solely by dissecting individual cells or proteins. And because the emergent, hierarchical organization masks much of the underlying biophysics, the cellular workings of the amplifier cannot be uniquely determined from the mechanical response. Although this ultimate "inverse problem" remains ill posed, inverse methods such as those outlined here (see also Zweig, 1991; de Boer, 1995a) may nonetheless offer invaluable guidance during the two-pronged pursuit. They provide, in effect, invertible functional transformations of the data $[V_{\mathrm{BM}} \rightleftarrows (\kappa,\gamma)]$ that bring the mechanistic constraints those data impose more fully and directly into view.

ACKNOWLEDGMENTS

We thank Nigel Cooper, Marcel van der Heijden, Philip Joris, Ombeline de La Rochefoucauld, Elizabeth Olson, Alberto Recio-Spinoso, Tianying Ren, Mario Ruggero, and Andrei Temchin for generously sharing their data. We also thank Christopher Bergevin, Egbert de Boer, Paul Fahey, John Guinan, Ombeline de La Rochefoucauld, Jeffery Lichtenhan, Robert Withnell, and the two anonymous reviewers for valuable comments on the manuscript. This work was supported by grant R01 DC03687 from the NIDCD, National Institutes of Health.

[1]Both the physiological vulnerability and nonlinearity of mammalian cochlear mechanics could be achieved without cycle-by-cycle power amplification (negative damping) if outer hair cells (OHCs) serve primarily to modify the reactive (rather than the resistive) component of the BM impedance (cf. Kolston *et al.*, 1990). An example would be if the stiffness of the partition were to depend on the dc component of OHC receptor potentials (e.g., Allen, 2001).

[2]The inversion procedure earns its name because it solves an "inverse problem"—it obtains the values of model parameters (in this case, the propagation and gain functions) directly from experimental data.

[3]The subtracted exponential map [Eq. (4)] is equivalent to Greenwood's (1990) equation

$$\mathrm{CF}(x) = A[10^{a(1-x/L)} - k].$$

The parameters are related by $\mathrm{CF}(0)=A(10^{a}-k)$, $\mathrm{CF}_{\mathrm{I}}=Ak$, and $l=L/(a\ln 10)$. (Greenwood's parameter k is a dimensionless constant and should not be confused with the wave number.) Approximate parameter values for the species {chinchilla, cat, gerbil} considered here are $\mathrm{CF}(0)=\{20.4,57,62.8\}$ kHz, $\mathrm{CF}_{\mathrm{I}}=\{0.14,0.365,0.25\}$ kHz, and $l=\{3.8,5.17,2.19\}$ mm (Liberman, 1982; Greenwood, 1990; Müller, 1996).

[4]At fixed location, Eq. (5) implies that $\Delta\beta=[1+\beta_1(x)]\Delta\nu$. If $\Delta\nu$ represents the (fixed) width of the function $V_{\mathrm{BM}}[\nu(x_o),f)]$ when plotted on a ν axis, then the quality factor $[Q=\mathrm{CF}(x_o)/\Delta f]$ of the transfer function is given by $1/Q=\Delta\beta=[1+\beta_1(x)]\Delta\nu$. As a result, Q decreases and the transfer function broadens as the value of $\beta_1(x_o)$ increases toward the apex.

[5]In the two-dimensional model, the averaged pressure $\bar{P}(x,f)$ is defined by

$$\bar{P}(x,f) \equiv \frac{1}{H}\int_0^H P(x,y,f)dy,$$

where H is the scalae height. The difference pressure is defined by $P(x,y) \equiv p(x,y) - p(x,-y)$, where $p(x,y)$ is the scala pressure (i.e., the scala-vestibuli pressure for $y>0$ and the scala-tympani pressure for $y<0$). The pressure difference is antisymmetric about the partition: $P(x,-y) = -P(x,y)$.

[6]To relate these apical boundary conditions to the velocity of the stapes (oval window), we evaluate $\partial_x \bar{P}$ at $x=0$ using Eq. (8). The result is

$$\partial_x \bar{P}|_{x=0} = -bZ_f \int_0^L V_{BM}(x,f)dx.$$

The linearized Euler equation implies that

$$\partial_x \bar{P}|_{x=0} = -Z_f U_{ow},$$

where U_{ow} is the volume velocity of the oval window (Shera *et al.*, 2005). Together, these two equations imply that the oval-window volume velocity equals the total (integrated) volume velocity of the BM:

$$U_{ow}(f) = b\int_0^L V_{BM}(x,f)dx.$$

When evaluated using experimental data, the integral on the right-hand side might be termed the "virtual stapes volume velocity" (cf. de Boer and Nuttall, 1999).

[7]Problems with branch cuts can be minimized by defining the square root as $\sqrt{z(x)} = \sqrt{|z(x)|}e^{i\theta(x)/2}$, where $\theta(x)$ is the *unwrapped* phase of $z(x)$.

[8]An example using plane waves with constant amplitude and wavelength may be helpful. Consider the (standing) wave $P(x) = \cos[k(x-L)]$, which can be represented as a superposition of forward- and reverse-traveling components:

$$P(x) = \tfrac{1}{2}[e^{-ik(x-L)} + e^{+ik(x-L)}].$$

If the function $V(x)$ is related to $P(x)$ by the differential equation $V(x) = \partial_x^2 P(x)$, then $V(x) = -k^2 P(x)$ and the wave number can be found using the formula $k^2 = -V(x)/P(x)$. When given only $V(x)$, one can find $P(x)$ by double integration:

$$P(x) = 1 + \int_x^L dx' \int_{x'}^L V(x'')dx'',$$

where the constants and limits of integration have been chosen to satisfy the boundary conditions [in this example, $P(L)=1$ and $\partial_x P(L)=0$]. The formula $k^2 = -V/P$ for the wavenumber then yields

$$k^2 = -V(x) \Bigg/ \left[1 + \int_x^L dx' \int_{x'}^L V(x'')dx''\right],$$

a result easily verified by direct substitution of the value $V(x) = -k^2\cos[k(x-L)]$.

[9]About half (27/51) of the remaining Wiener kernels gave fair reconstructions; the rest were very bad.

[10]Performing causal fits (e.g., Zweig, 1991) to the ensemble of functions yielded results almost identical to those obtained using loess (see Sec. III D).

[11]Although the result is more general, Eq. (12) is easily derived for the two-dimensional box model. The total time-averaged power $W(x,f)$ passing the point x towards the helicotrema is given by

$$W(x,f) = \tfrac{1}{2}b\,\mathrm{Re}\int Pu^* dy,$$

where $u(x,y)$ is the x component of the fluid particle velocity; b is the scala width; and the integral is over the scala height. The time-average power per unit BM area transfered to the traveling pressure-difference wave from the organ of Corti is given by $1/b$ times the spatial derivative of $W(x,f)$:

$$w(x,f) = \frac{1}{b}\partial_x W(x,f) = \tfrac{1}{2}\,\mathrm{Re}\int u^*\partial_x P + P\partial_x u^* dy.$$

The first term in the integrand can be eliminated using the linearized Euler equation $[\partial_x P = -2i\omega\rho_0 u]$. Substitution yields $-2i\omega\rho_0|u|^2$, which is purely imaginary and does not contribute to the real part of the integral that defines the power transfer. The second term can be simplified by evaluating $\partial_x u$ using the Euler equation and applying Laplace's equation $[(\partial_x^2 + \partial_y^2)P = 0]$. The result is

$$w(x,f) = -\frac{1}{4\omega\rho_0}\,\mathrm{Im}\int P\partial_y^2 P^* dy.$$

The integration can be done by parts. Putting in the limits of integration yields

$$\int P\partial_y^2 P^* dy = P\partial_y P^*\Big|_0^H - \int |\partial_y P|^2 dy.$$

The second term on the right-hand side is real and drops out when taking the imaginary part indicated above. The contribution from the boundary at $y=H$ vanishes because the vertical component of the fluid velocity, and hence $\partial_y P$, must be zero at the ceiling. At the cochlear partition the particle velocity must equal the BM velocity; hence $\partial_y P|_{y=0+} = 2i\omega\rho_0 V_{BM}$. Putting it all together yields Eq. (12):

$$w(x,f) = -\tfrac{1}{2}\,\mathrm{Re}\,P_0 V_{BM}^*,$$

where $P_0(x) \equiv P(x, y=0^+)$ is the pressure across the cochlear partition.

[12]More generally, the impedance and wave number are related by $Z_{BM} = -\alpha Z_f/k^2$ [Shera *et al.*, 2005, Eq. (20)], where $\alpha \equiv P_0/\bar{P}$. Equation (13) therefore becomes

$$w(x,f) = -\omega\rho_0 H|V_{BM}|^2\,\mathrm{Im}\frac{\alpha}{(kH)^2},$$

where we have used the definition $Z_f = 2i\omega\rho_0/bH$. In the shortwave regime ($|kH|>1$) near the response peak, $\alpha \to kH$, and the power transfer simplifies to the value given in Eq. (14).

[13]To compute the values $\mathcal{P}_\uparrow$ shown in Fig. 15 (and the ratios $\mathcal{P}_\uparrow/\mathcal{P}_\downarrow$ in Fig. 17), we used the general formula for $w(x,f)$ given in Note 12, approximating α using the WKB approximation: $\alpha_{WKB} = kH/\tanh kH$ (Shera *et al.*, 2005). Values of the scalae height H were obtained from the measurements reported by Salt (2001) for chinchilla and Wysocki (2001) for cat.

[14]When computing $\mathcal{P}_\uparrow$ the BM with was assumed constant, consistent with the assumed model geometry. Although the BM width varies slowly along the cochlea, it remains approximately constant over the region of the wave peak, where the dominant contributions to the net power arise. Had changes in BM width been included in the calculation, the values of $\mathcal{P}_\uparrow$ shown in Fig. 15 would increase by roughly another factor of 3 from base to apex.

[15]The Kramers–Krönig dispersion relations are also known as Hilbert transforms, depending on context.

[16]The overall signs of the Kramers–Krönig relations given in Eqs. (16) and (17) differ from those in many references (e.g., Mathews and Walker, 1964; Lucarini *et al.*, 2005). The signs depend on the sign convention chosen for the time-domain Fourier transform, which, confusingly, has not been standardized across fields. Physicists use one convention, engineers the other. For historical reasons related to telephony, auditory physics has adopted the engineering convention.

[17]To obtain Eqs. (16) and (17) the more general Kramers–Krönig equations were simplified by assuming that $k(\nu) = k^*(-\nu)$, where $*$ represents complex conjugation. The existence of the integrals also requires that $\kappa(\nu)$ and $\gamma(\nu)$ vanish as ν approaches infinity.

[18]Note further that the group delay can only rigorously be interpreted as the physical delay of a wave packet (or "group") when the corresponding amplitude function is constant over the band of interest (e.g., Papoulis, 1962). This condition fails in the cutoff region, where the wave amplitude changes rapidly.

[19]van der Heijden and Joris (2006) estimate the wavelength of the traveling wave by fitting a regression line to the spatial phase profile in the "slow propagation region" near the characteristic place. The values they obtain agree well with values of $2\pi/\kappa$ averaged over the peak region.

[20]Although we focus here on the *power gain* of the amplifier, other measures

of gain have been employed in the literature (reviewed in Robles and Ruggero, 2001; de Boer and Nuttall, 2001).

[21]Chinchilla stimulus-frequency emissions (SFOAEs) evoked by low-intensity pure tones have mean levels about 20 dB below the stimulus (Siegel *et al.*, 2005). However, because of the substantial variability across frequency and between subjects, SFOAE and ANF measurements in the same animals are needed to quantify the validity of the no-emission approximation ($\mathcal{P}_{\Leftarrow} \cong 0$) in individual ears. The task is further complicated by variability in forward and reverse middle-ear transmission (Songer and Rosowksi, 2007). Since we lack the measurements needed to fully resolve the issue, we simply note that Eq. (27) overestimates the power gain in ears that produce significant stimulus reemission.

[22]The ratio G/G_{passive} provides a measure of power gain that partially accounts for the effects of passive losses. (G_{passive} is the value of G measured in the same preparation after the active elements have been disabled.) The accounting is imperfect because at fixed stimulus level (i.e., fixed $\mathcal{P}_{\Rightarrow}$) the passive losses themselves depend on BM velocity and therefore vary with G.

[23]Note that the dip in the power ratios evident near 2 kHz in Fig. 17 corresponds to the frequency region where chinchilla SFOAEs, and presumably their emitted power, are generally the smallest (Siegel *et al.*, 2005). This observation is consistent with the fact that emitted power ($\mathcal{P}_{\Leftarrow} > 0$) increases the value of r.

[24]In fact, the bandwidths are so narrow that they are called "linewidths."

[25]Although compelling evidence suggests that the backward-traveling waves involved in the production of SOAEs are slow, pressure-difference waves (Nuttall *et al.*, 2004), both slow and fast (i.e., compressional) waves "reflect" (i.e., produce forward-traveling slow waves) at the stapes (e.g., Shera *et al.*, 2007). Thus, the production of intracochlear standing waves—and the subsequent emergence of laser-like oscillations from the ear—does not depend, in principle, on the mechanisms or speed of reverse propagation.

Allen, J. B. (**2001**). "Nonlinear cochlear signal processing," *Physiology of the Ear*, edited by A. F. Jahn and J. Santos-Sacchi (Singular, San Diego, CA), pp. 393–442.

Bialek, W., and Wit, H. P. (**1984**). "Quantum limits to oscillator stability: Theory and experiments on acoustic emissions from the human ear," Phys. Lett. **104A**, 173–178.

Bode, H. (**1945**). *Network Analysis and Feedback Amplifier Design* (Van Nostrand Reinhold, Princeton, NJ).

Cleveland, W. S. (**1993**). *Visualizing Data* (Hobart Press, Summit, NJ).

Cody, A. R. (**1992**). "Acoustic lesions in the mammalian cochlea: Implications for the spatial distribution of the 'active process'," Hear. Res. **62**, 166–172.

Cooper, N. P., and Rhode, W. S. (**1995**). "Nonlinear mechanics at the apex of the guinea-pig cochlea," Hear. Res. **82**, 225–243.

de Boer, E. (**1983**). "No sharpening? A challenge for cochlear mechanics," J. Acoust. Soc. Am. **73**, 567–579.

de Boer, E. (**1995a**). "The 'inverse problem' solved for a three-dimensional model of the cochlea. I. Analysis," J. Acoust. Soc. Am. **98**, 896–903.

de Boer, E. (**1995b**). "The 'inverse problem' solved for a three-dimensional model of the cochlea. II. Application to experimental data sets," J. Acoust. Soc. Am. **98**, 904–910.

de Boer, E. (**1996**). "Mechanics of the cochlea: Modeling efforts," *The Cochlea*, edited by P. Dallos, A. N. Popper, and R. R. Fay (Springer, New York), pp. 258–317.

de Boer, E. (**1997a**). "Classical and non-classical models of the cochlea," J. Acoust. Soc. Am. **101**, 2148–2150.

de Boer, E. (**1997b**). "Cochlear models and minimum phase," J. Acoust. Soc. Am. **102**, 3810–3813.

de Boer, E. (**1997c**). "Connecting frequency selectivity and nonlineary for models of the cochlea," Aud. Neurosci. **3**, 377–388.

de Boer, E., and Nuttall, A. L. (**1999**). "The 'inverse problem' solved for a three-dimensional model of the cochlea. III. Brushing-up the solution method," J. Acoust. Soc. Am. **105**, 3410–3420.

de Boer, E., and Nuttall, A. L. (**2001**). "Power gain of the cochlear amplifier," *Physiological and Psychological Bases of Auditory Function*, edited by D. J. Breebaart, A. J. M. Houtsma, A. Kohlrausch, V. F. Prijs, and R. Schoonhoven (Shaker, Maastricht), pp. 1–7.

de La Rochefoucauld, O., and Olson, E. S. (**2007**). "The role of organ of Corti mass in passive cochlear tuning," Biophys. J. in press.

Duifhuis, H. (**1988**). "Cochlear macromechanics," *Auditory Function: Neurological Bases for Hearing*, edited by G. M. Edelman, W. E. Gall, and W. M. Cowan (Wiley, New York), pp. 189–212.

Eggermont, J. J. (**1993**). "Wiener and Volterra analyses applied to the auditory system," Hear. Res. **66**, 177–201.

Eldredge, D. H., Miller, J. D., and Bohne, B. A. (**1981**). "A frequency-position map for the chinchilla cochlea," J. Acoust. Soc. Am. **69**, 1091–1095.

Geisler, C. D., and Sang, C. (**1995**). "A cochlear model using feed-forward outer-hair-cell forces," Hear. Res. **86**, 132–146.

Georgi, H. (**1993**). *The Physics of Waves* (Prentice-Hall, Englewood Cliffs, NJ).

Ghaffari, R., Aranyosi, A. J., and Freeman, D. M. (**2007**). "Longitudinally propagating traveling waves of the mammalian tectorial membrane," Proc. Natl. Acad. Sci. U.S.A. in press.

Golay, M. J. E. (**1961**). "Note on coherence vs narrow-bandedness in regenerative oscillators, masers, lasers, etc," Proc. IRE **49**, 958–959.

Greenwood, D. D. (**1990**). "A cochlear frequency-position function for several species—29 years later," J. Acoust. Soc. Am. **87**, 2592–2605.

Guinan, J. J., Lin, T., and Cheng, H. (**2005**). "Medial-olivocochlear-efferent inhibition of the first peak of auditory-nerve responses: Evidence for a new motion within the cochlea," J. Acoust. Soc. Am. **118**, 2421–2433.

Gummer, A. W., Smolders, J. W. T., and Klinke, R. (**1987**). "Basilar membrane motion in the pigeon measured with the Mössbauer technique," Hear. Res. **29**, 63–92.

Karavitaki, K. D., and Mountain, D. C. (**2007**). "Evidence for outer hair cell driven oscillatory fluid flow in the tunnel of Corti," Biophys. J. **92**, 3284–3293.

Kemp, D. T. (**1979**). "Evidence of mechanical nonlinearity and frequency selective wave amplification in the cochlea," Arch. Oto-Rhino-Laryngol. **224**, 37–45.

Kemp, D. T. (**2002**). "Exploring cochlear status with otoacoustic emissions: The potential for new clinical applications," *Otoacoustic Emissions: Clinical Applications*, 2nd ed., edited by M. S. Robinette and T. J. Glattke (Thieme, New York), pp. 1–47.

Khanna, S. M., and Hao, L. F. (**1999**). "Reticular lamina vibrations in the apical turn of a living guinea pig cochlea," Hear. Res. **132**, 15–33.

Kiang, N. Y. S., and Moxon, E. C. (**1974**). "Tails of tuning curves of auditory-nerve fibers," J. Acoust. Soc. Am. **55**, 620–630.

Kolston, P. J., Viergever, M. A., de Boer, E., and Diependaal, R. J. (**1989**). "Realistic mechanical tuning in a micromechanical cochlear model," J. Acoust. Soc. Am. **86**, 133–140.

Kolston, P. J., Viergever, M. A., de Boer, E., and Smoorenburg, G. F. (**1990**). "What type of force does the cochlear amplifier produce?" J. Acoust. Soc. Am. **88**, 1794–1801.

Koshigoe, S., and Tubis, A. (**1982**). "Implications of causality, time-translation invariance, linearity, and minimum-phase behavior for basilar-membrane response functions," J. Acoust. Soc. Am. **71**, 1194–1200.

Kramers, H. A. (**1927**). "La diffusion de la lumiére par les atomes," *Atti del Congresso Internazionale dei Fisici* (Zanichelli, Bologna, Italy), Vol. **2**, pp. 545–547.

Krönig, R. (**1926**). "On the theory of dispersion of x-rays," J. Opt. Soc. Am. **12**, 547–557.

Liberman, M. C. (**1978**). "Auditory-nerve response from cats raised in a low-noise chamber," J. Acoust. Soc. Am. **63**, 442–455.

Liberman, M. C. (**1982**). "The cochlear frequency map for the cat: Labeling auditory-nerve fibers of known characteristic frequency," J. Acoust. Soc. Am. **72**, 1441–1449.

Liberman, M. C., and Kiang, N. Y. S. (**1978**). "Acoustic trauma in cats: Cochlear pathology and auditory-nerve activity," Acta Oto-Laryngol., Suppl. **358**, 1–63.

Lighthill, J. (**1981**). "Energy flow in the cochlea," J. Fluid Mech. **106**, 149–213.

Longfellow, E. W. (**1922**). *Random Memories* (Houghton Mifflin, Boston, MA).

Lucarini, V., Peiponen, K.-E., Saarinen, J. J., and Vartiainen, E. M. (**2005**). *Kramers-Kronig Relations in Optical Materials Research* (Springer, Berlin, Germany).

Mathews, J., and Walker, R. (**1964**). *Mathematical Methods of Physics* (Benjamin, New York).

Müller, M. (**1996**). "The cochlear place-frequency map for adult and developing Mongolian gerbil," Hear. Res. **94**, 148–156.

Nedzelnitsky, V. (**1980**). "Sound pressures in the basal turn of the cat cochlea," J. Acoust. Soc. Am. **68**, 1676–1689.

Neely, S. T. (**1983**). "The cochlear amplifier," *Mechanics of Hearing*, edited

by E. Boer and M. A. Viergever (Martinus Nijhoff, The Hague), pp. 111–118.
Nowotny, M., and Gummer, A. W. (**2006**). "Nanomechanics of the subtectorial space caused by electromechanics of cochlear outer hair cells," Proc. Natl. Acad. Sci. U.S.A. **103**, 2120–2125.
Nuttall, A. L., Grosh, K., Zheng, J., de Boer, E., Zou, Y., and Ren, T. (**2004**). "Spontaneous basilar membrane oscillation and otoacoustic emission at 15 kHz in a guinea pig," J. Assoc. Res. Otolaryngol. **5**, 337–348.
Papoulis, A. (**1962**). *The Fourier Integral and its Applications* (McGraw-Hill, New York).
Poe, E. A. (**1844**). "The purloined letter," *The Gift: A Christmas, New Year's, and Birthday Present, 1845*, edited by E. L. Carey and A. Hart (Carey and Hart, Philadelphia, PA), pp. 41–61.
Puria, S. (**2003**). "Measurements of human middle ear forward and reverse acoustics: Implications for otoacoustic emissions," J. Acoust. Soc. Am. **113**, 2773–2789.
Recio-Spinoso, A., Temchin, A. N., van Dijk, P., Fan, Y.-H., and Ruggero, M. A. (**2005**). "Wiener-kernel analysis of responses to noise of chinchilla," J. Neurophysiol. **93**, 3615–3634.
Ren, T. (**2002**). "Longitudinal pattern of basilar membrane vibration in the sensitive cochlea," Proc. Natl. Acad. Sci. U.S.A. **99**, 17101–17106.
Rhode, W. S. (**1971**). "Observations of the vibration of the basilar membrane in squirrel monkeys using the Mössbauer technique," J. Acoust. Soc. Am. **49**, 1218–1231.
Rhode, W. S., and Cooper, N. P. (**1996**). "Nonlinear mechanics in the apical turn of the chinchilla cochlea *in vivo*," Aud. Neurosci. **3**, 101–121.
Robles, L., and Ruggero, M. A. (**2001**). "Mechanics of the mammalian cochlea," Physiol. Rev. **81**, 1305–1352.
Russell, I. J., and Kössl, M. (**1999**). "Micromechanical responses to tones in the auditory fovea of the greater mustached bat's cochlea," J. Neurophysiol. **82**, 676–686.
Russell, I. J., and Nilsen, K. E. (**1997**). "The location of the cochlear amplifier: Spatial representation of a single tone on the guinea pig basilar membrane," Proc. Natl. Acad. Sci. U.S.A. **94**, 2660–2664.
Salt, A. N. (**2001**). "Cochlear fluids simulator v1.6h," ⟨http://oto.wustl.edu/cochlea/model.htm⟩. Last viewed 9/26/07.
Santos-Sacchi, J. (**2000**). "Cell coupling in Corti's organ," Brain Res. Rev. **32**, 167–171.
Shera, C. A. (**2001**). "Frequency glides in click responses of the basilar membrane and auditory nerve: Their scaling behavior and origin in traveling-wave dispersion," J. Acoust. Soc. Am. **109**, 2023–2034.
Shera, C. A. (**2003a**). "Mammalian spontaneous otoacoustic emissions are amplitude-stabilized cochlear standing waves," J. Acoust. Soc. Am. **114**, 244–262.
Shera, C. A. (**2003b**). "Wave interference in the generation of reflection- and distortion-source emissions," *Biophysics of the Cochlea: From Molecules to Models*, edited by A. W. Gummer (World Scientific, Singapore), pp. 439–453.
Shera, C. A., and Guinan, J. J. (**2003**). "Stimulus-frequency-emission group delay: A test of coherent reflection filtering and a window on cochlear tuning," J. Acoust. Soc. Am. **113**, 2762–2772.
Shera, C. A., and Guinan, J. J. (**2007**). "Mechanisms of mammalian otoacoustic emission," *Active Processes and Otoacoustic Emissions in Hearing*, edited by G. A. Manley, R. R. Fay, and A. N. Popper (Springer, New York), in press.
Shera, C. A., Guinan, J. J., and Oxenham, A. J. (**2007**). "Otoacoustic estimates of cochlear tuning: Validation in the chinchilla," Assoc. Res. Otolaryngol. Abs. **30**, 519.
Shera, C. A., Tubis, A., and Talmadge, C. L. (**2005**). "Coherent reflection in a two-dimensional cochlea: Short-wave versus long-wave scattering in the generation of reflection-source otoacoustic emissions," J. Acoust. Soc. Am. **118**, 287–313.
Shera, C. A., Tubis, A., Talmadge, C. L., de Boer, E., Fahey, P. F., and Guinan, J. J. (**2007**). "Allen–Fahey and related experiments support the predominance of cochlear slow-wave otoacoustic emissions," J. Acoust. Soc. Am. **121**, 1564–1575.
Shera, C. A., and Zweig, G. (**1991**). "Reflection of retrograde waves within the cochlea and at the stapes," J. Acoust. Soc. Am. **89**, 1290–1305.
Siegel, J. H., Cerka, A. J., Recio-Spinoso, A., Temchin, A. N., van Dijk, P., and Ruggero, M. A. (**2005**). "Delays of stimulus-frequency otoacoustic emissions and cochlear vibrations contradict the theory of coherent reflection filtering," J. Acoust. Soc. Am. **118**, 2434–2443.
Siegman, A. E. (**1986**). *Lasers* (University Science Books, Sausalito, CA), Errata available at ⟨http://www.stanford.edu/~siegman⟩. Last viewed 9/26/07.
Songer, J. E., and Rosowksi, J. J. (**2007**). "Transmission matrix analysis of the chinchilla middle ear," J. Acoust. Soc. Am. **122**, 932–942.
Steele, C. R., Baker, G., Tolomeo, J., and Zetes, D. (**1993**). "Electromechanical models of the outer hair cell," *Biophysics of Hair Cell Sensory Systems*, edited by H. Duifhuis, J. W. Horst, P. van Dijk, and S. M. van Netten (World Scientific, Singapore), pp. 207–214.
Talmadge, C. L., Tubis, A., Long, G. R., and Piskorski, P. (**1998**). "Modeling otoacoustic emission and hearing threshold fine structures," J. Acoust. Soc. Am. **104**, 1517–1543.
Talmadge, C. L., Tubis, A., and Tong, C. (**2001**). "Cochlear wave reflection due to roughness in 2-D and 3-D cochlear models," Assoc. Res. Otolaryngol. Abs. **24**, 44.
Temchin, A. N., Recio-Spinoso, A., van Dijk, P., and Ruggero, M. A. (**2005**). "Wiener kernels of chinchilla auditory-nerve fibers: Verification using responses to tones, clicks, and noise and comparison with basilar-membrane vibrations," J. Neurophysiol. **93**, 3635–3648.
Thiers, F. A., Burgess, B. J., and Nadol, J. B. (**2002**). "Reciprocal innervation of outer hair cells in a human infant," J. Assoc. Res. Otolaryngol. **3**, 269–278.
Toll, J. S. (**1956**). "Causality and the dispersion relation: Logical foundations," Phys. Rev. **104**, 1760–1770.
van der Heijden, M., and Joris, P. X. (**2003**). "Cochlear phase and amplitude retrieved from the auditory nerve at arbitrary frequencies," J. Neurosci. **23**, 9194–9198.
van der Heijden, M., and Joris, P. X. (**2006**). "Panoramic measurements of the apex of the cochlea," J. Neurosci. **26**, 11462–11473.
von Békésy, G. (**1960**). *Experiments in Hearing* (McGraw-Hill, New York).
Wysocki, J. (**2001**). "Dimensions of the vestibular and tympanic scalae of the cochlea in selected mammals," Hear. Res. **161**, 1–9.
Zinn, C., Maier, H., Zenner, H. P., and Gummer, A. W. (**2000**). "Evidence for active, nonlinear, negative feedback in the vibration response of the apical region of the in vivo guinea-pig cochlea," Hear. Res. **142**, 159–183.
Zweig, G. (**1976**). "Basilar membrane motion," *Cold Spring Harbor Symposia on Quantitative Biology*, (Cold Spring Harbor Laboratory, Cold Spring Harbor, NY), Vol. **XL**, pp. 619–633.
Zweig, G. (**1991**). "Finding the impedance of the organ of Corti," J. Acoust. Soc. Am. **89**, 1229–1254.
Zweig, G., Lipes, R., and Pierce, J. R. (**1976**). "The cochlear compromise," J. Acoust. Soc. Am. **59**, 975–982.
Zweig, G., and Shera, C. A. (**1995**). "The origin of periodicity in the spectrum of evoked otoacoustic emissions," J. Acoust. Soc. Am. **98**, 2018–2047.
Zwiebach, B. (**2004**). *A First Course in String Theory* (Cambridge University Press, Cambridge, UK).